Journal of Computational Physics 305 (2016) 722–743

Contents lists available at ScienceDirect

Journal of Computational Physics

www.elsevier.com/locate/jcp

A combined finite element and oversampling multiscale Petrov–Galerkin method for the multiscale elliptic problems with singularities

Fei Song [1], Weibing Deng [*,2], Haijun Wu [3]

Department of Mathematics, Nanjing University, Nanjing 210093, People's Republic of China

ARTICLE INFO

Article history:
Received 6 April 2015
Received in revised form 23 September 2015
Accepted 7 November 2015
Available online 10 November 2015

Keywords:
Multiscale problems
Interface penalty
Combined finite element and oversampling multiscale Petrov–Galerkin method
Well-singularity

ABSTRACT

In this paper, we construct a combined finite element and oversampling multiscale Petrov–Galerkin method (FE-OMsPGM) to solve the multiscale problems which may have singularities in some special portions of the computational domain. For example, in the simulation of subsurface flow, singularities lie in the porous media with channelized features, or in near-well regions since the solution behaves like the Green function. The basic idea of FE-OMsPGM is to utilize the traditional finite element method (FEM) directly on a fine mesh of the problematic part of the domain and using the Petrov–Galerkin version of oversampling multiscale finite element method (OMsPGM) on a coarse mesh of the other part. The transmission condition across the FE-OMsPG interface is treated by the penalty technique. The FE-OMsPGM takes advantages of the FEM and OMsPGM, which uses much less DOFs than the standard FEM and may be more accurate than the OMsPGM for problems with singularities. Although the error analysis is carried out under the assumption that the oscillating coefficients are periodic, our method is not restrict to the periodic case. Numerical examples with periodic and random highly oscillating coefficients, as well as the multiscale problems on the L-shaped domain, and multiscale problems with high contrast channels or well-singularities are presented to demonstrate the efficiency and accuracy of the proposed method.

1. Introduction

In this paper, we consider the numerical simulation of second order elliptic problems with highly oscillating and strongly heterogeneous coefficients. This kind of problems, generally referred to as multiscale problems, are often used to describe the models arising in composite materials and flows in porous media. Due to the highly heterogeneous fine scale structure in the whole computational domain, it is extremely challenging to solve these problems numerically. The standard finite element method (FEM) usually requires very fine meshes and hence tremendous amount of computer memory and CPU time. To overcome the lack of performance of standard FEMs in cases where the coefficients have high variations, many

* Corresponding author.
E-mail addresses: songfei@smail.nju.edu.cn (F. Song), wbdeng@nju.edu.cn (W. Deng), hjw@nju.edu.cn (H. Wu).

[1] The work of this author was partially supported by the University Postgraduate Research and Innovation Project of Jiangsu Province 2014 under Grant KYZZ_0021.
[2] The work of this author was partially supported by the National Natural Science Foundation of China Grant 10971096, and by the PAPD.
[3] The work of this author was partially supported by the National Natural Science Foundation of China Grants 11071116, 91130004.

http://dx.doi.org/10.1016/j.jcp.2015.11.013
0021-9991/

multiscale numerical methods have been developed and studied in the past several decades, see e.g. [1–12]. Most of them are designed to solve the multiscale problems on meshes that are coarser than the scale of oscillations. The small-scale effect on the coarse scale is either captured by localized multiscale basis functions or modeled into the coarse-scale equations with a prescribed analytical form. The resulting modified coarse problem can then be solved numerically and its solution contains crucial information from the fine scales.

In this paper, we focus on the multiscale finite element method (MsFEM) introduced in [13–15], which aims to construct the multiscale basis functions from the local solutions of the elliptic operator for finite element formulation. Many extensions and applications of the MsFEM have been done in the past fifteen years. See for example, the MsFEMs for nonlinear problems [16,17], the MsFEM for two phase flow in porous media [18], the MsFEMs using limited global information [19], the Petrov–Galerkin version of MsFEM using the conforming test functions [20], the mixed MsFEM [21–24], the modified MsFEM for advection diffusion equations presented in [25], the multiscale finite volume method for subsurface flow simulation proposed in [26], the MsFEMs for elliptic interface problems with high contrast coefficients [27] and for solving high-contrast problems using local spectral basis functions [28]. We refer the reader to the book [29] for more discussions on the theory and applications of MsFEMs.

It is shown in [15] that the classical MsFEM suffers from a so called resonance error which manifests as a ratio between the characteristic size of the small scale and the mesh size of the coarse grid; the error becomes large when these two scales are close. There are two different sources accounting for this error. The first one is the mismatch between the local boundary conditions imposed for the basis functions and the global nature of the oscillatory solution, which can be effectively removed by using an oversampling technique [14]. The second source of scale resonance is due to the mismatch between the mesh size and the "perfect" sample size. In the periodic case, the "perfect" sample size should be some multiple of the periodic cell. It has been found that the Petrov–Galerkin version of MsFEM can eliminate this cell resonance error completely by using the oversampling technique to construct the basis functions but using the conforming piecewise linear functions as test functions (see [20]). In the periodic setting, the paper [30] proposed a regularization of the local problems by adding a zero-order term, which can reduce both sources of the resonance error significantly. We remark that a new oversampling strategy based on an additional constrained for the solution spaces of the local problems can prevent resonance errors even for general L^∞ coefficients without any assumptions such as periodicity or scale separation (see [31]).

However, in a lot of applications, the multiscale problems may have singularities in some special portions of the computational domain, such as, high contrast channels that connect the boundaries of coarse-grid blocks [28,32–34], or the Dirac function singularities which stems from the simulation of steady flow transport through highly heterogeneous porous media driven by extraction wells [35]. The standard FEM or oversampling MsFEM/MsPGM may be inefficient for this class of problems. Consequently, there has been a lot of work on the numerical methods for such problems. See for example, the MsFEMs by use of local spectral basis functions for high-contrast problems [28], an adaptive generalized MsFEM for high-contrast flow problems [36], a complete multiscale coarse grid algorithm by using the Green functions for solving steady flow problem involving well singularities in heterogeneous porous medium [35]. In this paper, we concentrate on a rather recent approach called the combined finite element and oversampling multiscale finite element method (FE-OMsFEM) that was proposed by W. Deng and H. Wu [37], which uses the standard FEM on a fine mesh of the problematic part of the domain and the oversampling MsFEM on a coarse mesh of the other part. The transmission condition on the interface between coarse and fine meshes is dealt with the penalty technique (see [38–41]). In general, they deal with the transmission condition on the interface by penalizing the jumps from the function values as well as the fluxes of the finite element solution on the fine mesh to those of the oversampling multiscale finite element solution on the coarse mesh. It is shown [37] that the FE-OMsFEM can solve the multiscale elliptic problems with fine and long-ranged high contrast channels or the well singularities very efficiently.

In this paper, we are concerned with the combination of the traditional FEM and the Petrov–Galerkin version of MsFEM. Note that the traditional FEM has many excellences to deal with the singularities, such as, refining the mesh or enlarging the polynomial order of the FE space. At the same time, the Petrov–Galerkin method can decrease the computational complexity significantly, allowing for more efficient solution algorithms. Furthermore, the Petrov–Galerkin version of MsFEM has no nonconforming error due to the conforming piecewise linear test space. Thus, in order to take advantages of both methods, we introduce a combined finite element and oversampling multiscale Petrov–Galerkin method (FE-OMsPGM) to solve the multiscale problems which may have singularities. The idea of this new approach is to utilize the traditional FEM directly on a fine mesh of the problematic part of the domain and use the OMsPGM on a coarse mesh of the other part, which is closely related to the FE-OMsFEM. The transmission condition across the FE-OMsPG interface is treated by the penalty technique. Although the penalty term of the fluxes is the same as that of the FE-OMsFEM, we deal with the jump term of the solution in a new function expression between the coarse and fine meshes. Comparing to the implement of FE-OMsFEM, there are two key issues of the FE-OMsPGM to consider. The first one is how to define its bilinear form, which needs to use the transfer operator between the approximation space and the test function space. We emphasis that the bilinear form of FE-OMsPGM introduced in this paper is not just a direct extension of FE-OMsFEM that replaces the multiscale test function space with the conforming piecewise linear function space. More delicate choice of the terms of bilinear form should be made. The second one is how to show the inf-sup condition or coercive condition of the bilinear form.

We remark that although the theoretical analysis is based on the homogenization theory under the assumption that the oscillating coefficient is periodic, our method is not restrict to the periodic case. The numerical results show that the introduced FE-OMsPGM is very efficient for random generated coefficients. Recently, the multiscale methods on localization

of the elliptic multiscale problems with highly varying (non-periodic) coefficients are studied in some papers. For instance, the new variational multiscale methods are presented in [42,43]; the discontinuous Galerkin multiscale methods for second order elliptic problems and convection–diffusion problems are proposed in [44,45]; a new oversampling strategy for the MsFEM is presented in [31]. In the future work, we will give more extensions and developments on our combined methods with the new oversampling strategy.

The remainder of this paper is organized as follows. In Section 2 we first present the model problem, and recall the OMsPGM for it, then derive the formulation of FE-OMsPGM. The Section 3 is devoted to error estimate of our method. It includes the homogenization theory, some preliminaries and the main result. In Section 4 we first give several numerical examples with periodic coefficients to demonstrate the accuracy of the method. Then we do some experiments to study how the size of oversampling elements affects the errors. Finally, we apply our method to multiscale problems on the L-shaped domain, to a multiscale problem which has fine and long-ranged high-contrast channels as well as the multiscale problems with well-singularity to demonstrate the efficiency of the method. Conclusions are drawn in the last section.

Throughout this paper, the Einstein summation convention is used: summation is taken over repeated indices. Standard notation on Lebesgue and Sobolev spaces is employed. Subsequently $C, C_0, C_1, \cdots$ denote generic constants, which are independent of ϵ, H, h and d, unless otherwise stated. We also use the shorthand notation $A \lesssim B$ and $B \lesssim A$ for the inequality $A \le CB$ and $B \le CA$. The notation $A \eqsim B$ is equivalent to the statement $A \lesssim B$ and $B \lesssim A$.

2. FE-OMsPGM formulation

Let $\Omega \subset \mathbf{R}^n$, $n = 2, 3$ be a polyhedral domain, and consider the following elliptic model problem:

$$\begin{cases} -\nabla \cdot (\mathbf{a}^\epsilon(x)\nabla u_\epsilon(x)) = f(x) & \text{in } \Omega, \\ u_\epsilon(x) = 0 & \text{on } \partial\Omega, \end{cases} \tag{2.1}$$

where $\epsilon \ll 1$ is a small parameter characterizing the small scale in the physical problem, $f \in L^2(\Omega)$, $a_{ij}^\epsilon \in L^\infty(\Omega)$, $1 \le i, j \le n$, and $\mathbf{a}^\epsilon(x) = (a_{ij}^\epsilon(x))$ is a symmetric, positive definite matrix:

$$\lambda|\xi|^2 \le a_{ij}^\epsilon(x)\xi_i\xi_j \le \Lambda|\xi|^2 \quad \forall \xi \in \mathbf{R}^n,\ x \in \bar{\Omega} \tag{2.2}$$

for some positive constants λ and Λ.

In the following subsection we first briefly describe the Petrov–Galerkin version of oversampling MsFEM for the model problem (cf. [20,29]). Then, we introduce our combined FE and OMsPG method for the multiscale problem.

2.1. OMsPGM for the model problem

Let $\mathcal{T}_H$ be a shape-regular and quasi-uniform triangulation of the domain Ω. To recall the OMsPGM for (2.1), we need the oversampling MsFE space on $\mathcal{T}_H$ defined as follows (cf. [46,14,29]). For any $K \in \mathcal{T}_H$ with nodes $\{x_i^K\}_{i=1}^{n+1}$, let $\{\varphi_i^K\}_{i=1}^{n+1}$ be the basis of $P_1(K)$ satisfying $\varphi_i^K(x_j^K) = \delta_{ij}$, $1 \le i, j \le n+1$, where δ_{ij} stands for the Kronecker's symbol. For any $K \in \mathcal{T}_H$, we denote by $S = S(K)$ a macro-element (simplex) which contains K, and ∂S is away from ∂K at some distance $d_{S(K)} := \mathrm{dist}(K, \partial S)$ (to be specified later). See Fig. 3 for an illustration.

Denote by $\{\varphi_i^S\}_{i=1}^{n+1}$ the nodal basis of $P_1(S)$ such that $\varphi_i^S(x_j^S) = \delta_{ij}$, $1 \le i, j \le n+1$, where x_j^S are vertices of S. Let $\psi_i^S \in H^1(S)$, $i = 1, \cdots, n+1$, be the solution of the problem:

$$-\nabla \cdot (\mathbf{a}^\epsilon \nabla \psi_i^S) = 0 \qquad \text{in } S, \qquad \psi_i^S|_{\partial S} = \varphi_i^S. \tag{2.3}$$

The oversampling multiscale finite element basis functions over K are defined by

$$\bar{\psi}_i^K = \sum_{j=1}^{n+1} c_{ij}^K \psi_j^S|_K \qquad \text{in } K, \qquad i = 1, \cdots, n+1, \tag{2.4}$$

with the constants c_{ij}^K determined by

$$\varphi_i^K = \sum_{j=1}^{n+1} c_{ij}^K \varphi_j^S|_K \qquad \text{in } K, \qquad i = 1, \cdots, n+1. \tag{2.5}$$

The existence of the constants c_{ij}^K is guaranteed because $\{\varphi_j^S\}_{j=1}^{n+1}$ forms a basis of $P_1(K)$.

Let $\mathrm{OMS}(K) = \mathrm{span}\{\bar{\psi}_i^K\}_{i=1}^{n+1}$ be the set of space functions on K. Define the projection $\Pi_K : \mathrm{OMS}(K) \to P_1(K)$ as

$$\Pi_K \psi = c_i \varphi_i^K \qquad \text{if} \qquad \psi = c_i \bar{\psi}_i^K \in \mathrm{OMS}(K).$$

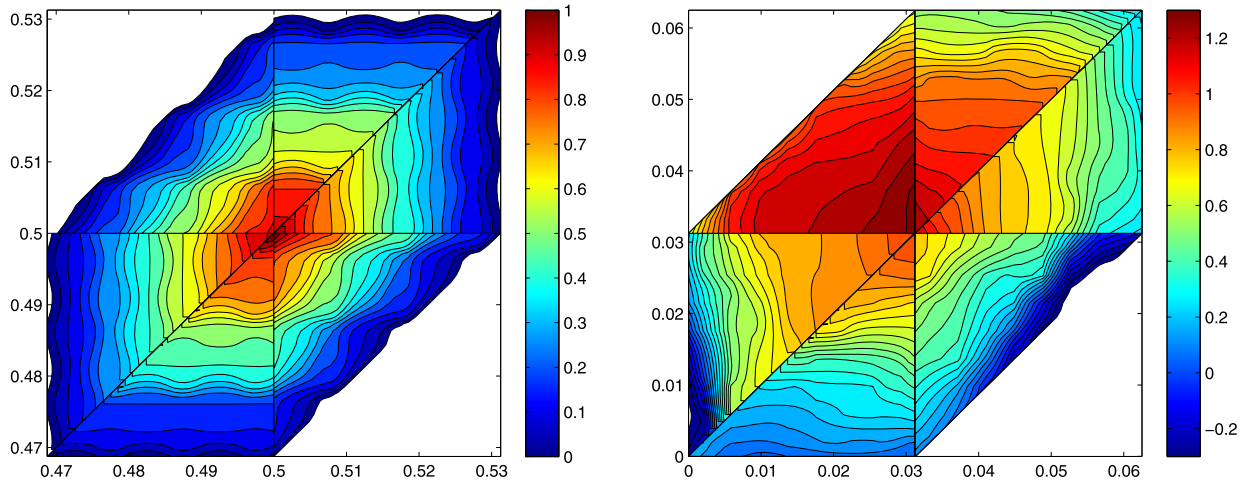

Fig. 1. Example of oversampling basis functions. Left: basis function for periodic media. Right: basis function for random media.

Introduce the space of discontinuous piecewise "OMS" functions and the space of discontinuous piecewise linear functions:

$$V_{H,dc}^{ms} = \{\psi_H : \ \psi_H|_K \in \mathrm{OMS}(K) \ \ \forall K \in \mathcal{T}_H\},$$
$$V_{H,dc} = \{v_H : \ v_H|_K \in P_1(K) \ \ \forall K \in \mathcal{T}_H\}.$$

Here we use the abbreviated indexes 'ms', 'dc', and 'nc' for multiscale, discontinuous and nonconforming, respectively. Define $\Pi_H : V_{H,dc}^{ms} \to V_{H,dc}$ through the relation

$$\Pi_H \psi_H|_K = \Pi_K \psi_H \ \text{ for any } K \in \mathcal{T}_H, \psi_H \in V_{H,dc}^{ms}.$$

The oversampling multiscale finite element space on $\mathcal{T}_H$ is then defined as

$$V_{H,nc}^{ms} = \{\psi_H \in V_{H,dc}^{ms} : \Pi_H \psi_H \in V_H \subset H_0^1(\Omega)\},$$

where $V_H = V_{H,dc} \cap H_0^1(\Omega)$ is the H^1-conforming linear finite element space over $\mathcal{T}_H$. In general, $V_{H,nc}^{ms} \not\subset H_0^1(\Omega)$ and the requirement $\Pi_H \psi_H \in V_H$ is to impose certain continuity of the functions $\psi_H \in V_{H,nc}^{ms}$ across the inter-element boundaries. Noting that $\Pi_K \bar{\psi}_i^K = \varphi_i^K$, the condition of $\Pi_H \psi_H \in V_H$ is satisfied if the global degrees of freedom are taken at the vertices of the mesh. For illustrations of some multiscale basis functions, we refer to Fig. 1.

Hence, the oversampling MsPGM is defined as follows: Find $U_H^{ms} \in V_{H,nc}^{ms}$ such that:

$$\sum_{K \in \mathcal{T}_H} \int_K \mathbf{a}^\epsilon \nabla U_H^{ms} \cdot \nabla v \, \mathrm{d}x = \int_\Omega f v \, \mathrm{d}x \quad \forall v \in V_H.$$

2.2. FE-OMsPGM formulation

In this subsection we present the combined FE and OMsPG method for the model problem. We always assume that there is no coefficient information available outside of the computing domain. We first separate the computational domain Ω into two parts Ω_1 and Ω_2 such that Ω_1 is the union of sub-domains where we will use the traditional FEM and Ω_2 is the union of sub-domains where we will use the oversampling MsPGM. For our setting, we always have $\Omega_2 \subset\subset \Omega$ and $\Omega = \Omega_1 \cup \Omega_2 \cup \Gamma$, where $\Gamma = \partial\Omega_1 \cap \partial\Omega_2$ is the interface of Ω_1 and Ω_2 (see Fig. 2 for an illustration). Note that we put the elements adjacent to the boundary $\partial\Omega$ into Ω_1 and use the traditional FEM there to avoid using the outside information of the coefficient.

Remark 1. It is easy to see that the OMsPG cell problem (2.3) defining in the boundary element (element adjacent to the boundary) utilizes the coefficient information outside of the research domain. There are several approaches to deal with this issue besides using the traditional FEM near the boundary. One is to use the classical MsFE space (without oversampling) instead of the oversampling one in the elements adjacent to the boundary, while to apply oversampling MsFE space to the inside elements. We call this method as the mixed basis MsPGM. Another one is to modify the definition of the oversampling elements near the boundary as follows. The oversampling domain $\tilde{K}$ for the boundary element K would simply be $S(K) \cap \Omega$, and the boundary condition for the oversampling domain would be the same boundary condition for $\partial\Omega \cap \partial\tilde{K}$, which, for example, may be chosen as linear boundary condition on $\partial\tilde{K} \setminus \partial\Omega$.

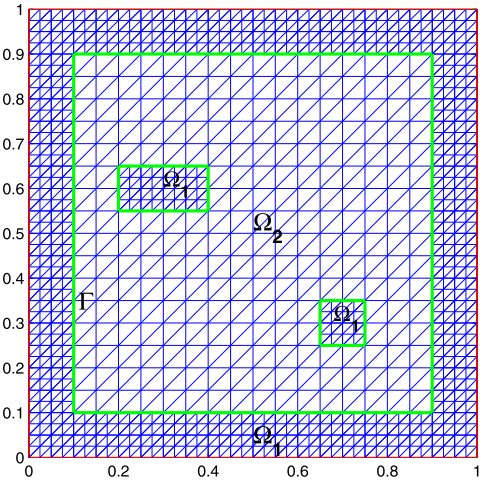

Fig. 2. A separation of the domain and a sample mesh.

The authors think both approaches do not affect the convergence order of the classical oversampling MsPGM because they only change the classical oversampling bases in a very small region (with measure $O(H)$). But both of them perform worse in our numerical experiments than either the classical oversampling MsPGM (which uses coefficients outside the computational domain) or the FE-OMsPGM.

For simplicity, we assume that the length/area of Γ satisfies $|\Gamma| = O(1)$, and Γ is Lipschitz continuous. Let $\mathcal{T}_{h,1}$ and $\mathcal{T}_{H,2}$ be the shape-regular and quasi-uniform triangulations of the domain Ω_1 and Ω_2 respectively, and denote Γ_h and Γ_H the two partitions of the interface Γ induced by $\mathcal{T}_{h,1}$ and $\mathcal{T}_{H,2}$, respectively. For any element $K \in \mathcal{T}_{h,1}$ (or $K \in \mathcal{T}_{H,2}$), we define h_K (or H_K) as $\mathrm{diam}(K)$. Similarly, for each edge/face e of $K_e \in \mathcal{T}_{h,1}$ (or E of $K_E \in \mathcal{T}_{H,2}$), define h_e as $\mathrm{diam}(e)$ (or H_E as $\mathrm{diam}(E)$). Denote by $h = \max_{K\in\mathcal{T}_{h,1}} h_K$ and $H = \max_{K\in\mathcal{T}_{H,2}} H_K$. We assume that, for $h < H$, on the interface Γ, $\mathcal{T}_{H,2}$ and $\mathcal{T}_{h,1}$ satisfy the matching condition that Γ_h is a refinement of Γ_H. Clearly, each edge/face in Γ_H is composed of some edges/faces in Γ_h. Combining the two triangulations together, we define $\mathcal{T}_{h,H}$ as the triangulation of Ω (see Fig. 2 for an illustration of triangulation).

For any point on Γ, we associate a unit normal $\mathbf{n}$, which is oriented from Ω_1 to Ω_2. For any piecewise H^1 function v over $\mathcal{T}_{h,H}$, denote by $v_i := v|_{\Omega_i}$, $i = 1, 2$, and define the jump $[v]$ and average $\{v\}$ on the interface Γ as

$$[v] := v_1|_\Gamma - v_2|_\Gamma, \qquad \{v\} := \frac{v_1|_\Gamma + v_2|_\Gamma}{2}, \tag{2.6}$$

where $v_i|_\Gamma, i = 1, 2$, are the traces of v_i on the interface Γ.

To present the FE-OMsPGM formulation, we introduce the following "energy" space:

$$V := \left\{ v : \ v|_{\Omega_i} = v_i, \ \text{ where } v_i \in H_0^1(\Omega) \cap H^s(\Omega),\ i = 1, 2 \right\},\ s > \frac{3}{2}. \tag{2.7}$$

Testing the elliptic problem (2.1) by any $v \in V$, using integration by parts, and using the identity $[vw] = \{v\}[w] + [v]\{w\}$, we obtain the weak formulation of (2.1):

$$\sum_{i=1}^{2} \int_{\Omega_i} \mathbf{a}^\epsilon \nabla u_\epsilon \cdot \nabla v \, \mathrm{d}x - \int_\Gamma \left\{ \mathbf{a}^\epsilon \nabla u_\epsilon \cdot \mathbf{n} \right\} [v] \, \mathrm{d}s = \int_\Omega f v \, \mathrm{d}x. \tag{2.8}$$

From now on, the spaces that only have an index H are restricted to Ω_2, the spaces with only index h are restricted to Ω_1 and the spaces with both H and h are defined on the whole Ω. Similar to the OMsPGM in Subsection 2.1, we introduce the space of discontinuous piecewise "OMS" functions and the space of discontinuous piecewise linear functions on $\mathcal{T}_{H,2}$:

$$V_{H,dc}^{ms} = \{\psi_H : \ \psi_H|_K \in \mathrm{OMS}(K) \ \ \forall K \in \mathcal{T}_{H,2}\},$$
$$V_{H,dc} = \{v_H : \ v_H|_K \in P_1(K) \ \ \forall K \in \mathcal{T}_{H,2}\}.$$

Define $\Pi_H : V_{H,dc}^{ms} \to V_{H,dc}$ through the relation:

$$\Pi_H \psi_H|_K = \Pi_K \psi_H \ \text{ for any } K \in \mathcal{T}_{H,2}, \psi_H \in V_{H,dc}^{ms}.$$

The oversampling multiscale finite element space on $\mathcal{T}_{H,2}$ is then defined as

$$V_{H,nc}^{ms} = \{\psi_H \in V_{H,dc}^{ms} : \Pi_H \psi_H \in V_H \subset H^1(\Omega_2)\},$$

where $V_H = V_{H,dc} \cap H^1(\Omega_2)$ is the H^1-conforming linear finite element space over $\mathcal{T}_{H,2}$.

Denote by V_h the H^1-conforming linear finite element space over $\mathcal{T}_{h,1}$ and denote

$$V_h^0 := \{v_h \in V_h :\ v_h = 0 \text{ on } \partial\Omega_1 / \Gamma\}. \tag{2.9}$$

We define the FE-OMsPGM approximation space $V_{h,H}^{ms}$ as

$$V_{h,H}^{ms} := \left\{\psi_{h,H} :\ \psi_{h,H}|_{\Omega_1} = \psi_h, \psi_{h,H}|_{\Omega_2} = \psi_H,\ \text{ where } \psi_h \in V_h^0,\ \psi_H \in V_{H,nc}^{ms}\right\}. \tag{2.10}$$

And denote the test function space $V_{h,H}$ as

$$V_{h,H} := \left\{v_{h,H} :\ v_{h,H}|_{\Omega_1} = v_h, v_{h,H}|_{\Omega_2} = v_H,\ \text{ where } v_h \in V_h^0, v_H \in V_H\right\}. \tag{2.11}$$

Notice that $V_{h,H} \subset V$ is obvious.

To define the discrete bilinear form, we need the transfer operator $\Pi : V_{h,H}^{ms} \to V_{h,H}$ as follows:

$$(\Pi\psi_{h,H})|_K = \begin{cases} \Pi_K(\psi_{h,H}|_K), & \forall K \in \mathcal{T}_{H,2}; \\ \psi_{h,H}|_K, & \forall K \in \mathcal{T}_{h,1}, \end{cases} \quad \text{for any } \psi_{h,H} \in V_{h,H}^{ms}. \tag{2.12}$$

Remark 2. Since the trial function and the test function are not in the same space, it is necessary to connect the two spaces through the above transfer operator Π in the proof of coercive condition of the following bilinear form.

Define the discrete bilinear form $A_\beta(\cdot,\cdot)$ on $V_{h,H}^{ms} \times V_{h,H}^{ms}$:

$$\begin{aligned} A_\beta(u_{h,H}, v_{h,H}) &:= \sum_{K\in\mathcal{T}_{h,H}} \int_K \mathbf{a}^\epsilon \nabla u_{h,H} \cdot \nabla \Pi v_{h,H}\, \mathrm{d}x - \sum_{e\in\Gamma_h} \int_e \left\{\mathbf{a}^\epsilon \nabla u_{h,H} \cdot \mathbf{n}\right\} \left[\Pi v_{h,H}\right] \mathrm{d}s \\ &\quad + \beta \sum_{e\in\Gamma_h} \int_e \left[\Pi u_{h,H}\right] \left\{\mathbf{a}^\epsilon \nabla v_{h,H} \cdot \mathbf{n}\right\} \mathrm{d}s + J_0(u_{h,H}, v_{h,H}) + J_1(u_{h,H}, v_{h,H}), \\ J_0(u_{h,H}, v_{h,H}) &:= \sum_{e\in\Gamma_h} \frac{\gamma_0}{\rho} \int_e \left[\Pi u_{h,H}\right] \left[\Pi v_{h,H}\right] \mathrm{d}s, \\ J_1(u_{h,H}, v_{h,H}) &:= \sum_{e\in\Gamma_h} \gamma_1 \rho \int_e \left[\mathbf{a}^\epsilon \nabla u_{h,H} \cdot \mathbf{n}\right] \left[\mathbf{a}^\epsilon \nabla v_{h,H} \cdot \mathbf{n}\right] \mathrm{d}s, \end{aligned} \tag{2.13}$$

where β is a real number such as $-1, 0, 1$, and $\gamma_0, \gamma_1, \rho > 0$ will be specified later. Define further the linear form $F(\cdot)$ on $V_{h,H}^{ms}$:

$$F(v_{h,H}) := \int_\Omega f \Pi v_{h,H}\, \mathrm{d}x. \tag{2.14}$$

Then, our combined finite element and oversampling multiscale Petrov–Galerkin method is to find $u_{h,H} \in V_{h,H}^{ms}$ such that

$$A_\beta(u_{h,H}, v_{h,H}) = F(v_{h,H}) \qquad \forall v_{h,H} \in V_{h,H}^{ms}. \tag{2.15}$$

Remark 3. (a) The above FE-OMsPGM is not just a trivial extension of the FE-OMsFEM by simply replacing the test function $v_{h,H} \in V_{h,H}^{ms}$ in the formulation of the FE-OMsFEM with $\Pi v_{h,H}$. The design of the last three terms in A_β is tricky. As a matter of fact, we have tried numerically different possibilities of using Π (or not before each $u_{h,H}$ or $v_{h,H}$) before we found that the current form of A_β in (2.13) is the best one and, most importantly, the corresponding FE-OMsPGM can be analyzed theoretically.

(b) The parameter $\rho > 0$ satisfies that $\rho \le \epsilon$. In fact, it is chosen as ϵ in our later error analysis, while in practical computation, it may be chosen as the mesh size h.

In order to estimate the error of the FE-OMsPG solution, we introduce the following norm on the discrete space $V_{h,H}^{ms}$:

$$\|v_{h,H}\|_{1,h,H} := \Bigg(\sum_{K\in\mathcal{T}_{h,H}} \|(\mathbf{a}^\epsilon)^{1/2}\nabla v_{h,H}\|^2_{L^2(K)} + \sum_{e\in\Gamma_h} \frac{\rho}{\gamma_0} \left\|\{\mathbf{a}^\epsilon \nabla v_{h,H}\cdot\mathbf{n}\}\right\|^2_{L^2(e)} + \sum_{e\in\Gamma_h} \gamma_1 \rho \left\|\left[\mathbf{a}^\epsilon \nabla v_{h,H}\cdot\mathbf{n}\right]\right\|^2_{L^2(e)} + \sum_{e\in\Gamma_h} \frac{\gamma_0}{\rho} \left\|\left[\Pi v_{h,H}\right]\right\|^2_{L^2(e)} \Bigg)^{1/2}.$$

Noting that the operator Π is not defined for the exact solution u_ϵ, we introduce the following function to measure the error of the discrete solution:

$$E(v, v_{h,H}) := \Bigg(\sum_{K\in\mathcal{T}_{h,H}} \|(\mathbf{a}^\epsilon)^{1/2}\nabla(v - v_{h,H})\|^2_{L^2(K)} + \sum_{e\in\Gamma_h} \frac{\rho}{\gamma_0} \left\|\{\mathbf{a}^\epsilon \nabla(v - v_{h,H})\cdot\mathbf{n}\}\right\|^2_{L^2(e)} + \sum_{e\in\Gamma_h} \gamma_1 \rho \left\|\left[\mathbf{a}^\epsilon \nabla(v - v_{h,H})\cdot\mathbf{n}\right]\right\|^2_{L^2(e)} + \sum_{e\in\Gamma_h} \frac{\gamma_0}{\rho} \left\|\left[v - \Pi v_{h,H}\right]\right\|^2_{L^2(e)} \Bigg)^{1/2}$$
$$\forall v \in H^2(\Omega),\ v_{h,H} \in V_{h,H}^{ms}. \tag{2.16}$$

From the triangle inequality, it is clear that, for any $v \in H^2(\Omega)$, $v_{h,H}$, $w_{h,H} \in V_{h,H}^{ms}$,

$$E(v, v_{h,H}) \lesssim E(v, w_{h,H}) + \|w_{h,H} - v_{h,H}\|_{1,h,H}. \tag{2.17}$$

3. Error estimates for the FE-OMsPGM

In this section we derive the H^1 error estimate for the FE-OMsPGM in the case where $\beta = -1$. For other cases such as $\beta = 0, 1$, the analysis is similar and is omitted here. The convergence analysis is only done for the periodic coefficient case where we assume that $\mathbf{a}^\epsilon(x)$ has the form $\mathbf{a}(x/\epsilon)$, and $a_{ij}(y)$ is a periodic function in y in a unit cube Y.

Recall that in Section 2 we made some assumptions on the interface and partitions on it as follows:

(H1) The length/area of Γ satisfies $|\Gamma| = O(1)$, and Γ is Lipschitz continuous.
(H2) On the interface Γ, $\mathcal{T}_{H,2}$ and $\mathcal{T}_{h,1}$ satisfy the matching condition that Γ_h is a refinement of Γ_H.

For further error analysis, we still need the following assumptions and notations:

(H3) For some constant C_0, $\text{dist}\{\Gamma, \partial\Omega\} \geq C_0 H \geq h + 2\epsilon > 0$.
(H4) $a_{ij} \in W^{2,p}(Y)$ for $p > n$.
(H5) $h < \epsilon < H$.
(H6) $d_{S(K)} \geq C_0 H_K$, where $d_{S(K)} := \text{dist}(K, \partial S)$ and C_0 is the constant from (H3).

Here H, h are the coarse and fine mesh sizes respectively. When there is no influence on the dominance order of error estimates, we use frequently $\epsilon/H < 1$ and $h/\epsilon < 1$ to simplify the intermediate results upon the assumption (H5).

From (H3), we can define a narrow subdomain $\Omega_\Gamma \subset\subset \Omega$ surrounding Γ as

$$\Omega_\Gamma := \Gamma \cup \{x : x \in \Omega_1, \text{dist}(x, \Gamma) < h + 2\epsilon\} \cup \{x : x \in \Omega_2,\ \text{dist}(x, \Gamma) < H + 2\epsilon\}. \tag{3.1}$$

Furthermore, we introduce several concepts related to the interface Γ. Define the set of elements accompanying with the interface partition Γ_h (or Γ_H) as follows:

$$K_{\Gamma_h} := \{K \in \mathcal{T}_{h,1} :\ K \text{ has at least one edge/face in } \Gamma_h\}, \tag{3.2}$$
$$K_{\Gamma_H} := \{K \in \mathcal{T}_{H,2} :\ K \text{ has at least one edge/face in } \Gamma_H\}. \tag{3.3}$$

Clearly, from (H1), the number of elements in K_{Γ_h} is $O(\frac{1}{h^{n-1}})$ and the number of elements in K_{Γ_H} is $O(\frac{1}{H^{n-1}})$. Denote by

$$\Omega_{\Gamma_H} = \cup\{K : K \in K_{\Gamma_H}\}, \qquad \Omega_{\Gamma_h} = \cup\{K : K \in K_{\Gamma_h}\}. \tag{3.4}$$

From the definition of Ω_Γ (see (3.1)), it is clear that $\Omega_{\Gamma_H}, \Omega_{\Gamma_h} \subset \Omega_\Gamma$ and $\text{dist}(\Omega_{\Gamma_H}, \partial\Omega_\Gamma)$, $\text{dist}(\Omega_{\Gamma_h}, \partial\Omega_\Gamma) \geq 2\epsilon$, respectively.

3.1. Homogenization theory and multiscale expansion

It is shown that under some mild assumptions (e.g. (H4) above), u_ϵ converges weakly in H^1 to the solution of the homogenized equation (cf. [47,48]):

$$\begin{cases} -\nabla\cdot(\mathbf{a}^*\nabla u_0(x)) = f(x) & \text{in } \Omega, \\ u_0(x) = 0 & \text{on } \partial\Omega, \end{cases} \tag{3.5}$$

where

$$a^*_{ij} = \frac{1}{|Y|}\int_Y a_{ik}(y)\left(\delta_{kj} + \frac{\partial \chi^j}{\partial y_k}(y)\right) \mathrm{d}y. \tag{3.6}$$

Here χ^j is the periodic solution of the cell problem:

$$-\nabla_y\cdot(\mathbf{a}(y)\nabla_y\chi^j(y)) = \nabla_y\cdot(\mathbf{a}(y)\mathbf{e}_j), \quad j = 1,\cdots,n \tag{3.7}$$

with zero mean, i.e., $\int_Y \chi^j dy = 0$, and $\mathbf{e}_j$ is the unit vector in the jth direction.

In our analysis, we need the facts that $\left|\nabla\chi^j(x/\epsilon)\right| \lesssim \epsilon^{-1}$, $\left|\nabla^2\chi^j(x/\epsilon)\right| \lesssim \epsilon^{-2}$. Both of them follow from the periodicity, (H4), and the embedding $W^{2,p}(Y)$ in $W^{1,\infty}(Y)$ for $p > n$ (see [49, Theorem 15.1 in Chapter 3]).

Let θ_ϵ denote the boundary corrector which is the solution of

$$\begin{aligned} -\nabla\cdot(\mathbf{a}^\epsilon\nabla\theta_\epsilon) &= 0 && \text{in } \Omega, \\ \theta_\epsilon &= -\chi^j(x/\epsilon)\frac{\partial u_0(x)}{\partial x_j} && \text{on } \partial\Omega. \end{aligned} \tag{3.8}$$

From the Maximum Principle, we have

$$\|\theta_\epsilon\|_{L^\infty(\Omega)} \lesssim |u_0|_{W^{1,\infty}(\Omega)}. \tag{3.9}$$

In the following part, for convenience's sake, we will set

$$u_1(x, x/\epsilon) = u_0(x) + \epsilon\chi^j(x/\epsilon)\frac{\partial u_0(x)}{\partial x_j}. \tag{3.10}$$

Recall that ψ_i^S, $i = 1,\cdots,n+1$ are defined by (2.3). By the asymptotic expansion (cf. [13,20]), we know that

$$\psi_i^S = \varphi_i^S + \epsilon\chi^j(x/\epsilon)\frac{\partial\varphi_i^S}{\partial x_j} + \epsilon\eta^j(x)\frac{\partial\varphi_i^S}{\partial x_j},$$

with η^j being the solution of

$$-\nabla\cdot(\mathbf{a}^\epsilon\nabla\eta^j) = 0 \quad \text{in } S, \qquad \eta^j\big|_{\partial S} = -\chi^j(x/\epsilon). \tag{3.11}$$

Therefore the oversampling MsFE basis function $\bar{\psi}_i^K$ (see (2.4)) has the following expansion:

$$\bar{\psi}_i^K = \varphi_i^K + \epsilon\chi^j(x/\epsilon)\frac{\partial\varphi_i^K}{\partial x_j} + \epsilon\eta^j(x)\frac{\partial\varphi_i^K}{\partial x_j}, \tag{3.12}$$

where $\{\varphi_i^K\}_{i=1}^{n+1}$ are the bases of $P_1(K)$ satisfying $\varphi_i^K(x_j^K) = \delta_{ij}$.

By the Maximum Principle we have

$$\left\|\eta^j\right\|_{L^\infty(S)} \le \left|\chi^j\right|_{L^\infty(S)} \lesssim 1, \tag{3.13}$$

which together with the interior gradient estimate (see [37, Lemma 3.6] or [13, Proposition C.1]) imply that

$$\left\|\nabla\eta^j\right\|_{L^\infty(K)} \lesssim d_{S(K)}^{-1}\left\|\eta^j\right\|_{L^\infty(S)} \lesssim \frac{1}{d_{S(K)}}. \tag{3.14}$$

3.2. Preliminaries

We first recall a trace inequality which is a direct consequence of the standard trace inequality ([50, Theorem 1.6.6, p. 39]) and the scaling argument (cf. [51]).

Lemma 3.1. *Let K be an element of the triangulation $\mathcal{T}_{H,2}$ (or $\mathcal{T}_{h,1}$). Then, for any $v \in H^1(K)$, we have*

$$\|v\|_{L^2(\partial K)} \leq C\left(\operatorname{diam}(K)^{-1/2}\|v\|_{L^2(K)} + \|v\|_{L^2(K)}^{1/2}\|\nabla v\|_{L^2(K)}^{1/2}\right). \tag{3.15}$$

Next, we recall the stability estimate for Π_H, which will be used in our later analysis. The proof is similar to that of Lemma 5.1 in [37]. We arrange it in Appendix A.

Lemma 3.2. *Assume that (H4)–(H6) hold. Then there exist positive constants β_0, α_1 and α_2 which are independent of H and ϵ such that if $\epsilon/H_K \leq \beta_0$ for all $K \in \mathcal{T}_{H,2}$, then the following estimates are valid for all $v_H \in V_{H,nc}^{ms}$,*

$$\|\nabla v_H\|_{L^2(K)} \eqsim \|\nabla \Pi_H v_H\|_{L^2(K)}, \tag{3.16}$$

$$\alpha_2\|\nabla v_H\|_{L^2(K)}^2 \leq \left|\int_K \mathbf{a}^\epsilon \nabla v_H \cdot \nabla \Pi_H v_H\right| \leq \alpha_1\|\nabla v_H\|_{L^2(K)}^2. \tag{3.17}$$

The following lemma gives an inverse estimate for the function in space $\mathrm{OMS}(K)$ (see [37, Lemma 5.2]):

Lemma 3.3. *Under the assumptions of Lemma 3.2 we have the following estimate:*

$$|v_H|_{H^2(K)} \lesssim \frac{1}{\epsilon}\|\nabla v_H\|_{L^2(K)} \quad \forall\, v_H \in \mathrm{OMS}(K). \tag{3.18}$$

Since the convergence analysis is only done for the periodic coefficient case, we will fix $\rho = \epsilon$ in the later analysis. The following lemma gives the continuity and coercivity of the bilinear form $A_\beta(\cdot,\cdot)$ for the FE-OMsPGM:

Lemma 3.4. *We have*

$$\left|A_\beta(u_{h,H}, v_{h,H})\right| \leq C\left\|u_{h,H}\right\|_{1,h,H}\left\|v_{h,H}\right\|_{1,h,H} \qquad \forall\, u_{h,H}, v_{h,H} \in V_{h,H}^{ms}. \tag{3.19}$$

Further, let the assumptions of Lemma 3.3 be fulfilled. Then for any $0 < \gamma_1 \lesssim 1$, there exists a constant α_0 independent of h, H, ϵ, and γ_0, γ_1 such that, if $\gamma_0 \geq \alpha_0/\gamma_1$, then

$$A_\beta(v_{h,H}, v_{h,H}) \geq \kappa\left\|v_{h,H}\right\|_{1,h,H}^2 \qquad \forall\, v_{h,H} \in V_{h,H}^{ms}, \tag{3.20}$$

where $\kappa > 0$ is a constant independent of h, H, ϵ, γ_0, and γ_1.

Proof. From the definition of the norms, the Cauchy–Schwarz inequality and Lemma 3.2, it follows (3.19) immediately.

It remains to prove (3.20). From (3.17), we have

$$\begin{aligned} A_\beta(v_{h,H}, v_{h,H}) \geq C &\sum_{K\in\mathcal{T}_{h,H}}\left\|(\mathbf{a}^\epsilon)^{1/2}\nabla v_{h,H}\right\|_{L^2(K)}^2 - 2\sum_{e\in\Gamma_h}\int_e \left\{\mathbf{a}^\epsilon\nabla v_{h,H}\cdot\mathbf{n}\right\}\left[\Pi v_{h,H}\right] \\ &+ \sum_{e\in\Gamma_h}\frac{\gamma_0}{\epsilon}\left\|\left[\Pi v_{h,H}\right]\right\|_{L^2(e)}^2 + \sum_{e\in\Gamma_h}\gamma_1\epsilon\left\|\left[\mathbf{a}^\epsilon\nabla v_{h,H}\cdot\mathbf{n}\right]\right\|_{L^2(e)}^2. \end{aligned}$$

It is obvious that,

$$\begin{aligned} 2\sum_{e\in\Gamma_h}\int_e \left\{\mathbf{a}^\epsilon\nabla v_{h,H}\cdot\mathbf{n}\right\}\left[\Pi v_{h,H}\right] &\leq 2\sum_{e\in\Gamma_h}\left\|\left\{\mathbf{a}^\epsilon\nabla v_{h,H}\cdot\mathbf{n}\right\}\right\|_{L^2(e)}\left\|\left[\Pi v_{h,H}\right]\right\|_{L^2(e)} \\ &\leq \sum_{e\in\Gamma_h}\frac{\gamma_0}{2\epsilon}\left\|\left[\Pi v_{h,H}\right]\right\|_{L^2(e)}^2 + \sum_{e\in\Gamma_h}\frac{2\epsilon}{\gamma_0}\left\|\left\{\mathbf{a}^\epsilon\nabla v_{h,H}\cdot\mathbf{n}\right\}\right\|_{L^2(e)}^2. \end{aligned}$$

Hence, we obtain

$$A_\beta(v_{h,H}, v_{h,H}) \geq C \sum_{K\in\mathcal{T}_{h,H}} \left\| (\mathbf{a}^\epsilon)^{1/2}\nabla v_{h,H} \right\|^2_{L^2(K)} + \frac{1}{2}\sum_{e\in\Gamma_h} \frac{\gamma_0}{\epsilon} \left\| \left[\Pi v_{h,H}\right] \right\|^2_{L^2(e)} + \frac{1}{2}\sum_{e\in\Gamma_h} \frac{\epsilon}{\gamma_0} \left\| \left\{\mathbf{a}^\epsilon \nabla v_{h,H}\cdot\mathbf{n}\right\} \right\|^2_{L^2(e)}$$
$$+ \sum_{e\in\Gamma_h} \gamma_1 \epsilon \left\| \left[\mathbf{a}^\epsilon \nabla v_{h,H}\cdot\mathbf{n}\right] \right\|^2_{L^2(e)} - \frac{5}{2}\sum_{e\in\Gamma_h} \frac{\epsilon}{\gamma_0} \left\| \left\{\mathbf{a}^\epsilon \nabla v_{h,H}\cdot\mathbf{n}\right\} \right\|^2_{L^2(e)}. \tag{3.21}$$

Note that, for any $e\in\Gamma_h$,

$$\left\{\mathbf{a}^\epsilon \nabla v_{h,H}\cdot\mathbf{n}\right\}\Big|_e = (\mathbf{a}^\epsilon \nabla v_H)\cdot\mathbf{n} + \frac{1}{2}\left[\mathbf{a}^\epsilon \nabla v_{h,H}\cdot\mathbf{n}\right]\Big|_e,$$

where $v_H := (v_{h,H})|_{\Omega_2}$. Hence, by use of the inverse estimate (3.18), Lemma 3.1, and $\epsilon < H$, we have

$$\begin{aligned}
\sum_{e\in\Gamma_h} \frac{\epsilon}{\gamma_0} \left\| \{\mathbf{a}^\epsilon \nabla v_{h,H}\cdot\mathbf{n}\} \right\|^2_{L^2(e)} &= \sum_{e\in\Gamma_h} \frac{\epsilon}{\gamma_0} \left\| \mathbf{a}^\epsilon \nabla v_H\cdot\mathbf{n} + \frac{1}{2}[\mathbf{a}^\epsilon \nabla v_{h,H}\cdot\mathbf{n}] \right\|^2_{L^2(e)} \\
&\leq \sum_{E\in\Gamma_H} \frac{2\epsilon}{\gamma_0} \left\| \mathbf{a}^\epsilon \nabla v_H\cdot\mathbf{n} \right\|^2_{L^2(E)} + \sum_{e\in\Gamma_h} \frac{1}{2\gamma_1\gamma_0}\gamma_1\epsilon \left\| [\mathbf{a}^\epsilon \nabla v_{h,H}\cdot\mathbf{n}] \right\|^2_{L^2(e)} \\
&\leq \sum_{K_E} \frac{2C_1}{\gamma_0} \left\| (\mathbf{a}^\epsilon)^{\frac{1}{2}} \nabla v_H \right\|^2_{L^2(K_E)} + \sum_{e\in\Gamma_h} \frac{1}{2\gamma_1\gamma_0}\gamma_1\epsilon \left\| [\mathbf{a}^\epsilon \nabla v_{h,H}\cdot\mathbf{n}] \right\|^2_{L^2(e)},
\end{aligned} \tag{3.22}$$

where $K_E\in\mathcal{T}_{H,2}$ is the element containing E. Therefore, from (3.21) and (3.22), we have

$$A_\beta(v_{h,H}, v_{h,H}) \geq \left(C - \frac{5C_1\gamma_1}{\gamma_0\gamma_1}\right) \sum_{K\in\mathcal{T}_{h,H}} \left\| (\mathbf{a}^\epsilon)^{1/2}\nabla v_{h,H} \right\|^2_{L^2(K)} + \frac{1}{2}\sum_{e\in\Gamma_h} \frac{\gamma_0}{\epsilon} \left\| \left[\Pi v_{h,H}\right] \right\|^2_{L^2(e)}$$
$$+ \frac{1}{2}\sum_{e\in\Gamma_h} \frac{\epsilon}{\gamma_0} \left\| \left\{\mathbf{a}^\epsilon \nabla v_{h,H}\cdot\mathbf{n}\right\} \right\|^2_{L^2(e)} + \left(1 - \frac{5}{4\gamma_0\gamma_1}\right) \sum_{e\in\Gamma_h} \gamma_1\epsilon \left\| \left[\mathbf{a}^\epsilon \nabla v_{h,H}\cdot\mathbf{n}\right] \right\|^2_{L^2(e)}.$$

Noting that $\gamma_1 \lesssim 1$, there exists a constant $\alpha_0 > 0$ independent of h, H, ϵ such that if $\gamma_0\gamma_1 \geq \alpha_0$ then $\frac{5C_1\gamma_1}{\gamma_0\gamma_1} < \frac{C}{2}$ and $\frac{5}{4\gamma_0\gamma_1} \leq \frac{1}{2}$. Then by choosing $\kappa = \min(\frac{C}{2}, \frac{1}{2})$, it follows (3.20). This completes the proof. □

Remark 4. For the case where $\beta = 1$, the coercivity of A_β holds under the condition that $\gamma_0 \gtrsim 1/\gamma_1$ since the second and third terms of $A_\beta(v_{h,H}, v_{h,H})$ are canceled directly.

Next we give the following lemma which is an analogue of the Céa's lemma:

Lemma 3.5. *There exists a constant α_0 independent of h, H, ϵ, and γ_0, γ_1 such that for $0 < \gamma_1 \lesssim 1$, $\gamma_0 \geq \alpha_0/\gamma_1$, the following inequality holds:*

$$E(u_\epsilon, u_{h,H}) \lesssim \inf_{v_{h,H}\in V^{ms}_{h,H}} E(u_\epsilon, v_{h,H}), \tag{3.23}$$

where the error function E is defined in (2.16).

Proof. It is clear that by Lemma 3.4 we have

$$\begin{aligned}
\left\| u_{h,H} - v_{h,H} \right\|^2_{1,h,H} &\lesssim A_\beta(u_{h,H} - v_{h,H}, u_{h,H} - v_{h,H}) \\
&= A_\beta(u_{h,H}, u_{h,H} - v_{h,H}) - A_\beta(v_{h,H}, u_{h,H} - v_{h,H}) \\
&= (f, \Pi(u_{h,H} - v_{h,H})) - A_\beta(v_{h,H}, u_{h,H} - v_{h,H})
\end{aligned}$$

From the weak formulation (2.8), it follows that

$$(f, \Pi(u_{h,H} - v_{h,H})) = \sum_{K\in\mathcal{T}_{h,H}} \int_K \mathbf{a}^\epsilon \nabla u_\epsilon \cdot \nabla\Pi(u_{h,H} - v_{h,H})\,\mathrm{d}x - \sum_{e\in\Gamma_h} \int_e \left\{\mathbf{a}^\epsilon \nabla u_\epsilon\cdot\mathbf{n}\right\} \left[\Pi(u_{h,H} - v_{h,H})\right] \mathrm{d}s$$

Thus, noticing the facts that $[u_\epsilon] = 0$ and $[\mathbf{a}^\epsilon \nabla u_\epsilon\cdot\mathbf{n}] = 0$, we have

$$
\begin{aligned}
&(f, \Pi(u_{h,H} - v_{h,H})) - A_\beta(v_{h,H}, u_{h,H} - v_{h,H}) \\
&= \sum_{K\in\mathcal{T}_{h,H}} \int_K \mathbf{a}^\epsilon \nabla(u_\epsilon - v_{h,H}) \cdot \nabla \Pi(u_{h,H} - v_{h,H})\, \mathrm{d}x - \sum_{e\in\Gamma_h} \int_e \{\mathbf{a}^\epsilon \nabla(u_\epsilon - v_{h,H}) \cdot \mathbf{n}\} \left[\Pi(u_{h,H} - v_{h,H})\right] \mathrm{d}s \\
&\quad + \sum_{e\in\Gamma_h} \gamma_1 \epsilon \int_e \left[\mathbf{a}^\epsilon \nabla(u_\epsilon - v_{h,H}) \cdot \mathbf{n}\right] \left[\mathbf{a}^\epsilon \nabla(u_{h,H} - v_{h,H}) \cdot \mathbf{n}\right] \mathrm{d}s \\
&\quad + \sum_{e\in\Gamma_h} \int_e \{\mathbf{a}^\epsilon \nabla(u_{h,H} - v_{h,H}) \cdot \mathbf{n}\} \left[\Pi v_{h,H} - u_\epsilon\right] \mathrm{d}s - \sum_{e\in\Gamma_h} \frac{\gamma_0}{\epsilon} \int_e \left[\Pi v_{h,H} - u_\epsilon\right] \left[\Pi(u_{h,H} - v_{h,H})\right] \mathrm{d}s \\
&\lesssim E(u_\epsilon, v_{h,H}) \left\| u_{h,H} - v_{h,H} \right\|_{1,h,H}.
\end{aligned}
$$

Hence, we have

$$
\left\| u_{h,H} - v_{h,H} \right\|_{1,h,H} \lesssim E(u_\epsilon, v_{h,H}),
$$

which together with (2.17) yields

$$
E(u_\epsilon, u_{h,H}) \lesssim E(u_\epsilon, v_{h,H}) + \left\| u_{h,H} - v_{h,H} \right\|_{1,h,H} \lesssim E(u_\epsilon, v_{h,H}).
$$

This completes the proof of the lemma. □

3.3. Main result

Now, we are ready to present the main result of the paper which gives the error estimate for the FE-OMsPGM.

Theorem 3.1. *Let u_ϵ be the solution of (2.1), and let $u_{h,H}$ be the numerical solution computed using FE-OMsPGM defined by (2.15). Assume that $u_0 \in H^2(\Omega) \cap W^{1,\infty}(\Omega)$, $f \in L^2(\Omega)$ and $f|_{\Omega_\Gamma} \in H^1(\Omega_\Gamma)$, that the assumptions (H1)–(H6) hold, and that the penalty parameters satisfy $0 < \gamma_1 \lesssim 1$ and $\gamma_0 \geq \alpha_0/\gamma_1$. Then there exists a constant γ independent of H and ϵ such that if $\epsilon/H_K \leq \gamma$ for all $K \in \mathcal{T}_{H,2}$, the following error estimate holds:*

$$
\begin{aligned}
E(u_\epsilon, u_{h,H}) \lesssim &\left(\sqrt{\epsilon} + \frac{\epsilon}{d} + \frac{h}{\epsilon} |\Omega_1|^{1/2}\right) |u_0|_{W^{1,\infty}(\Omega)} + H \|u_0\|_{H^2(\Omega)} \\
&+ \frac{H^2}{\sqrt{\epsilon}} \frac{|u_0|_{H^2(\Omega_\Gamma)}}{\sqrt{|\Omega_\Gamma|}} + \epsilon^2 \|\nabla f\|_{L^2(\Omega_\Gamma)},
\end{aligned} \tag{3.24}
$$

where $d = \min_{K\in\mathcal{T}_{H,2}} d_{S(K)}$.

The proof is similar to that of Theorem 5.5 in [37]. We arrange it in Appendix A for the interested reader.

Remark 5. (a) The error bound consists of three parts: the first part of order $O\left(\sqrt{\epsilon} + \frac{\epsilon}{d} + H\right)$ from the oversampling MsPG approximation in Ω_2, the second part of order $O\left(\frac{h}{\epsilon}|\Omega_1|^{1/2}\right)$ from the FE approximation in Ω_1, and the third part $\frac{H^2}{\sqrt{\epsilon}} \frac{|u_0|_{H^2(\Omega_\Gamma)}}{\sqrt{|\Omega_\Gamma|}} + \epsilon^2 \|\nabla f\|_{L^2(\Omega_\Gamma)}$ from the penalizations on Γ.

(b) In [37], it is shown that the H^1 error between u_ϵ and the FE-OMsFEM solution has the oscillating term $\frac{\epsilon}{H}$. Here it is removed by the Petrov–Galerkin version of OMsFEM.

4. Numerical tests

In this section, we first do some numerical experiments to show the accuracy of the proposed FE-OMsPGM. And then we study how the size of oversampling elements affects the errors. At last, we show some numerical experiments which deal with the multiscale elliptic problems on the L-shaped domain, and the multiscale problems with high contrast channels or well-singularities to demonstrate the robustness and convincing of the proposed method. In all computations, we do not assume that the values of the diffusion coefficient are available outside of the computing domain. In order to illustrate the performance of our method, we also implement three other kinds of methods: FE-OMsFEM introduced in [37], the standard MsFEM in Petrov–Galerkin formulation (MsPGM), and mixed basis MsPGM (see Remark 1). We also show the results of the standard linear FEM on the corresponding coarse grid to get a feeling for the accuracy of the multiscale methods.

For the methods FE-OMsPGM, FE-OMsFEM and mixed basis MsPGM, the triangulation may be done by the same way as that of [37]. We recall the procedure as follows:

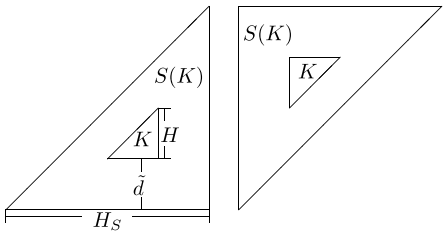

Fig. 3. The element K and its oversampling element $S(K)$: lower-right elements (left) and upper-left elements (right).

- First, we triangulate the domain Ω with a coarse mesh whose mesh size H is much bigger than ϵ.
- Secondly, we choose the union of coarse-grid elements adjacent to the boundary $\partial\Omega$ (and the channels or wells if exist) as Ω_1 and denote $\Omega \setminus \overline{\Omega_1}$ by Ω_2. For example, in our tests, we choose two layers of coarse-grid elements (and the coarse-grid elements containing the channels or wells if exist) to form the domain Ω_1. Hence the distance of Γ away from $\partial\Omega$ is $2H$.
- Finally, in Ω_2, we use the oversampling MsFE basis on coarse-grid elements. While, in Ω_1 we use the traditional linear FE basis on a fine mesh for the FE-OMsPGM (FE-OMsFEM), or use the standard MsFE basis on coarse-grid elements for the mixed basis MsPGM. In our tests, we fix the size of the fine mesh $h = 1/1024$ which is small enough to resolve the smallest scale of oscillations.

In the following tests, for simplicity, we use the standard triangulations on the subdomain Ω_2 (Ω_1), that is, $\mathcal{T}_{H,2}$ ($\mathcal{T}_{h,1}$) are constructed by first dividing the subdomain Ω_2 (Ω_1) into sub-squares of equal length H (h) and then connecting the lower-left and the upper-right vertices of each sub-square. Please see Fig. 2 for a sample standard triangulation. For any coarse-grid element $K \in \mathcal{T}_{H,2}$ we put its macro-element $S(K)$ in such a way such that their barycenters are coincide and their corresponding edges are parallel. We assume that all right-angle sides of $S(K)$, $K \in \mathcal{T}_{H,2}$ have the same length denoted by H_S. Let

$$\tilde{d} = (H_S - H)/3. \tag{4.1}$$

It is clear that $d \eqsim \tilde{d}$. See Fig. 3 for an illustration.

Since there are no exact solutions for the problems computed here, we will solve most of them on a very fine mesh with mesh size $h_f = 1/4096$ by use of the traditional linear finite element method and consider their numerical solutions as the "exact" solutions which are denoted as u_e. Denoting u_h as the numerical solutions computed by the methods considered in this section, we measure the relative error in L^2, L^∞ and energy norms as follows:

$$\frac{\|u_h - u_e\|_{L^2}}{\|u_e\|_{L^2}}, \quad \frac{\|u_h - u_e\|_{L^\infty}}{\|u_e\|_{L^\infty}}, \quad \frac{\|u_h - u_e\|_E}{\|u_e\|_E},$$

where

$$\|v\|_E := \left(\sum_{K \in \mathcal{T}_{H,2}} \|(\mathbf{a}^\epsilon)^{1/2} \nabla v\|^2_{L^2(K)} + \left\|(\mathbf{a}^\epsilon)^{1/2} \nabla v\right\|^2_{L^2(\Omega_1)} + \|v\|^2_{L^2(\Omega)} \right)^{1/2}.$$

In all tests, the coefficient $\mathbf{a}^\epsilon$ is chosen as the form $\mathbf{a}^\epsilon = a^\epsilon I$ where a^ϵ is a scalar function and I is the 2 by 2 identity matrix.

4.1. Accuracy of FE-OMsPGM

The purpose of the first numerical test is to demonstrate the accuracy of the FE-OMsPGM. To do this, we consider the model problem (2.1) in the squared domain $\Omega = [0,1] \times [0,1]$. Note that we set $\Omega_1 = \{x : \operatorname{dist}(x, \partial\Omega) < 2H\}$ and use the traditional FEM there to avoid using the outside information of the coefficient. Assume that $f = 1$ and the coefficient $\mathbf{a}^\epsilon(x_1, x_2)$ has the following periodic form:

$$\mathbf{a}^\epsilon(x_1, x_2) = \frac{2 + 1.8\sin(2\pi x_1/\epsilon)}{2 + 1.8\cos(2\pi x_2/\epsilon)} + \frac{2 + 1.8\sin(2\pi x_2/\epsilon)}{2 + 1.8\sin(2\pi x_1/\epsilon)}, \tag{4.2}$$

where we fix $\epsilon = 1/100$. In our FE-OMsPGM, we consider two choices of the parameter ρ. The first choice is $\rho = \epsilon$ as stated in our theoretical analysis, while the other one $\rho = h$, the size of the fine mesh. The second choice is useful when the scales are non-separable. We first choose $H = 1/32$ and report the relative errors in the L^2, L^∞ and energy norms in Table 1. We can see that the FE-OMsPGMs give the most accurate results among the methods considered here. Especially, when we take $\rho = h$, the FE-OMsPGM still works well. We also compare the CPU time T_1 and T_2 spent by the methods, where T_1 is the

Table 1
Compare different methods to show the accuracy of FE-OMsPGM in periodic case given by (4.2). $\epsilon = 1/100$, $\tilde{d} = H = 1/32$, $h = 1/1024$, $\gamma_0 = 20$, $\gamma_1 = 0.1$.

Relative error	L^2	L^∞	Energy norm	CPU time (s)	
				T_1	T_2
FEM	0.1150e−00	0.2311e−00	0.8790e−00	0.004	0.001
MsPGM	0.7448e−01	0.7342e−01	0.2929e−00	0.602	0.003
Mixed basis MsPGM	0.3596e−01	0.3656e−01	0.2255e−00	0.602	0.004
FE-OMsFEM ($\rho = \epsilon$)	0.1432e−01	0.1538e−01	0.1587e−00	0.950	1.466
FE-OMsPGM ($\rho = \epsilon$)	0.1178e−01	0.1275e−01	0.1583e−00	0.699	1.711
FE-OMsPGM ($\rho = h$)	0.1198e−01	0.1293e−01	0.1579e−00	0.699	1.711

Table 2
Convergence with respect to H. $\rho = \epsilon = 1/100$, $\tilde{d} = 1/32$, $h = 1/1024$, $\gamma_0 = 20$, $\gamma_1 = 0.1$.

Relative error	FE-OMsPGM		FE-OMsFEM	
	L^2	Energy norm	L^2	Energy norm
8×128	0.1844e−01	0.1676e−00	0.1863e−01	0.1676e−00
16×64	0.1490e−01	0.1640e−00	0.1507e−01	0.1640e−00
32×32	0.1178e−01	0.1583e−00	0.1432e−01	0.1587e−00
64×16	0.1232e−01	0.1577e−00	0.1015e−01	0.1710e−00

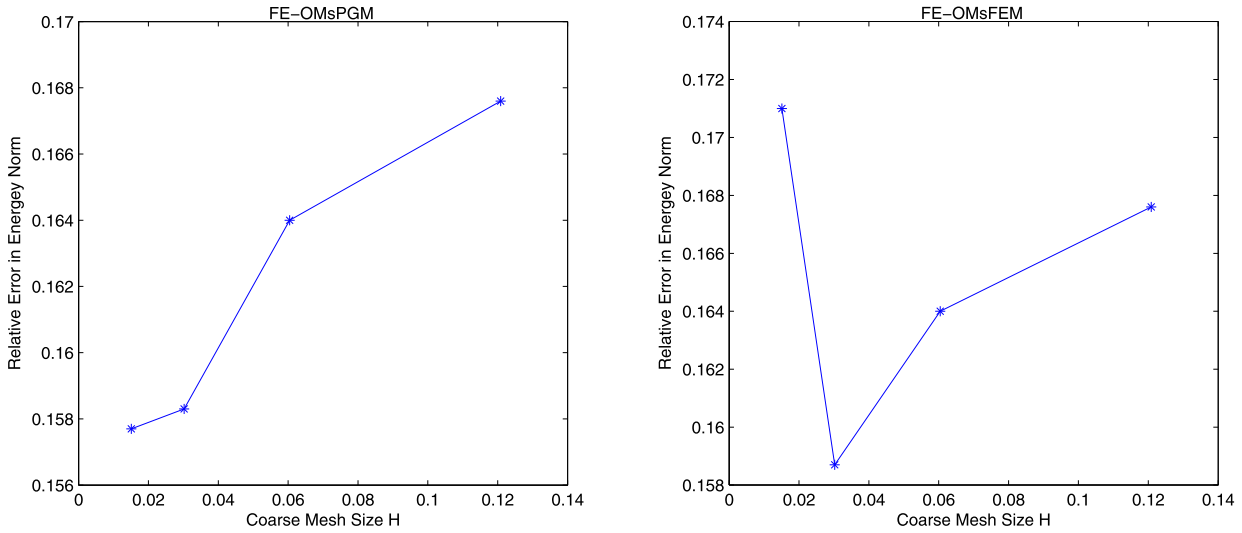

Fig. 4. Relative energy error against H.

CPU time of assembling the stiffness matrix, and T_2 is the CPU time of solving the discrete system of algebraic equations. Notice that the CPU time T_1 of our FE-OMsPGMs for assembling the stiffness matrix is shorter than that of FE-OMsFEM since the Petrov–Galerkin method can decrease the computational complexity significantly. But the CPU time T_2 for solving the linear system is a little longer which is due to the fact that the algebraic equation of PG version is nonsymmetric.

The second numerical experiment is to show the coarse mesh size H plays a role as that describing in Theorem 3.1. We fix $h = 1/1024$, $d = 1/32$ and $\epsilon = 1/100$. Four kinds of coarse mesh size are chosen. As for $H = 1/8$, it is denoted as 8×128. Other cases are similar. The results are shown in Table 2. It is easy to see that as H goes smaller, the relative error in energy norm goes smaller, which is in agreement with the theoretical results in Theorem 3.1. Relative error in energy norm against the distance H is clearly shown in Fig. 4. Note that this result is different from that of FE-OMsFEM in [37, Table 6.2], where the error estimate has the term ϵ/H due to the nonconforming error. In order to show the difference, we list the corresponding errors in Table 2 and plot the error in energy norm in Fig. 4 respectively. It is easy to see that as H goes larger, the relative error in energy norm of FE-OMsFEM goes lower first and goes higher later, which is in agreement with the fact its error has the nonconforming error ϵ/H.

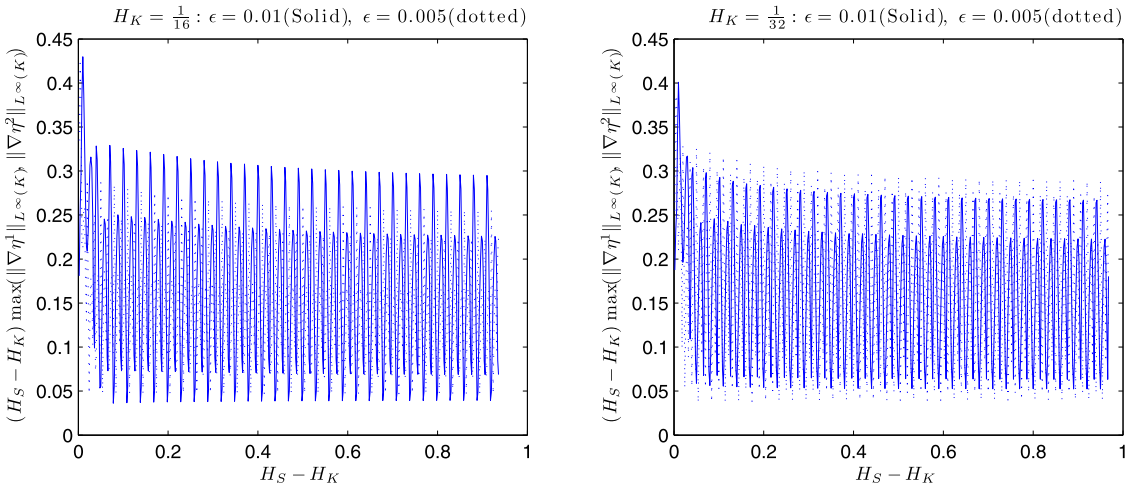

Fig. 5. Verification of (4.3) for $H_K = 1/16$ (left) and $H_K = 1/32$ (right).

Table 3
Error with respect to d. $\rho = \epsilon = 1/100$, $H = 1/32$, $h = 1/1024$, $\gamma_0 = 20$, $\gamma_1 = 0.1$.

Relative error	L^2	L^∞	Energy norm
$\tilde{d} = h = H/32$	0.34345e−01	0.38675e−01	0.19383e−00
$\tilde{d} = 2h = H/16$	0.25315e−01	0.28498e−01	0.17498e−00
$\tilde{d} = 4h = H/8$	0.17002e−01	0.18809e−01	0.16414e−00
$\tilde{d} = 8h = H/4$	0.12254e−01	0.14488e−01	0.15900e−00
$\tilde{d} = 16h = H/2$	0.11783e−01	0.13271e−01	0.15871e−00
$\tilde{d} = 32h = H$	0.11781e−01	0.12753e−01	0.15826e−00
$\tilde{d} = 64h = 2H$	0.10910e−01	0.11871e−01	0.15825e−00
$\tilde{d} = 96h = 3H$	0.10454e−01	0.11403e−01	0.15825e−00

4.2. Affection of the size of the oversampling patches

In this subsection we study how the size of oversampling elements affects the errors. For any $K \in \mathcal{T}_{H,2}$, we denote by $S = S(K)$ a macro-element (simplex) which contains K and ∂S is away from ∂K at some distance $d_{S(K)} := \text{dist}(K, \partial S)$. It is shown that the solution η^j of (3.11) satisfies (see also (3.14))

$$\left\|\nabla\eta^j\right\|_{L^\infty(K)} \lesssim \frac{1}{d_{S(K)}}. \tag{4.3}$$

The first experiment is to verify the above inequality for the model example with coefficient (4.2). $(H_S - H_K) \times \max_{j=1,2}\left\|\nabla\eta^j\right\|_{L^\infty(K)}$ is plotted in Fig. 5 for $H_K = 1/16, 1/32$, $\epsilon = 1/100, 1/200$ and different H_S, respectively. From the figures we can see that $\left\|\nabla\eta^j\right\|_{L^\infty(K)} \cdot d_{S(K)}$ are bounded by a constant from above which is consistent with (4.3).

The second numerical experiment is to show the distance $d = \min_{K\in\mathcal{T}_{H,2}} d_{S(K)}$ defined in the oversampling macro-element plays an important role as that describing in Theorem 3.1. We set $\rho = \epsilon = 1/100$, $H = 1/32$, $h = 1/1024$. The result is shown in Table 3. We can see that as $\tilde{d}$ (note $d \eqsim \tilde{d}$) goes larger, the relative error in energy norm goes smaller, which is coincided with the theoretical results in Theorem 3.1. We also notice that when $\tilde{d}$ is close to $\sqrt{\epsilon}$, the errors begin to decrease very slowly. Recall that there is a homogenization error $\sqrt{\epsilon}$ in the error estimate (3.24). We think that when d is large enough, $\sqrt{\epsilon}$ becomes the dominated error instead of ϵ/d.

4.3. Application to multiscale problems on the L-shape domain

In this subsection, we consider the multiscale problem on the L-shaped domain with the Dirichlet boundary condition. It is known that the solution has the singular behavior around reentrant corners. So the classical finite element method fails to provide satisfactory result.

We simulate the problems with periodic coefficient (4.2) and random log-normal permeability respectively. The random field $\mathbf{a}(x)$ is generated by using the moving ellipse average [52] with the variance of the logarithm of the permeability $\sigma^2 = 1.0$, and the correlation lengths $l_1 = l_2 = 0.01$ in x_1 and x_2 directions, respectively. One realization of the resulting random permeability field in our numerical experiments is depicted in Fig. 6. The results are shown in Table 4 and Table 5.

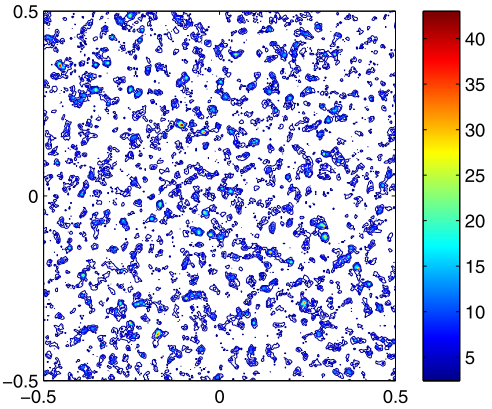

Fig. 6. The random log-normal permeability field $\mathbf{a}(x)$. $\frac{a_{\max}(x)}{a_{\min}(x)} = 2.9642\text{e}{+03}$.

Table 4
Relative errors for the L-shaped problem with periodic coefficient (4.2). $\rho = \epsilon = 1/100$, $h = 1/1024$, $\tilde{d} = H = 1/16$, $\gamma_0 = 10$, $\gamma_1 = 0.1$.

Relative error	L^2	L^∞	Energy norm
MsPGM	0.6937e−02	0.3448e−01	0.1989e−00
Mixed basis MsPGM	0.5130e−02	0.3063e−01	0.1326e−00
FE-OMsFEM	0.1428e−02	0.6731e−02	0.4282e−01
FE-OMsPGM	0.1669e−02	0.5252e−02	0.4162e−01

Table 5
Relative errors for the L-shaped problem with random coefficient $\sigma^2 = 1.0$ and $l_1 = l_2 = 0.01$. $\rho = h = 1/1024$, $\tilde{d} = H = 1/16$, $\gamma_0 = 10$, $\gamma_1 = 0.1$.

Relative error	L^2	L^∞	Energy norm
MsPGM	0.9089e−00	0.1303e+01	0.6486e+02
Mixed basis MsPGM	0.8885e−00	0.1483e+01	0.6307e+02
FE-OMsFEM	0.7427e−02	0.2747e−01	0.1513e−00
FE-OMsPGM	0.7596e−02	0.2424e−01	0.1045e−00

We can see that FE-OMsPGM gives a better approximation than the other three methods. Especially, for the random case, both standard MsPGM and mixed basis MsPGM give the wrong approximations to the gradient of solution.

4.4. Application to the multiscale problem with high-contrast channels

In this subsection, we use the FE-OMsPGM to solve the multiscale elliptic problem which has high-contrast channels inside the domain. In this test, we use the coefficient depicted in Fig. 7 that corresponds to a coefficient with background one and high permeability channels and inclusions with permeability values equal to 10^5 and 8×10^4 respectively. The problematic region is set within a (vertical or horizontal) distance of $2H$ from the channels. The results are listed in Table 6. We observe that our FE-OMsPGM gives much better results than those of MsPGM and mixed basis MsPGM, and gives better result than that of FE-OMsFEM in the energy norm.

4.5. Application to multiscale problems with the Dirac function singularities

In this subsection, we consider the elliptic multiscale problem with the Dirac function singularities inside the domain (see [35]).

We try to solve the following problem instead of the single phase pressure equation:

$$\begin{cases} -\nabla \cdot (\mathbf{a}^\epsilon(x)\nabla u(x)) = \sum_{j=1}^{2} q_j \delta_{\bar{x}_j} & \text{in } \Omega, \\ u(x) = 0 & \text{on } \partial\Omega, \end{cases} \tag{4.4}$$

where $\delta_{\bar{x}_j}$ is the Dirac measure at $\bar{x}_j$. The computations are performed on the unit square $\Omega = (0,1) \times (0,1)$. We consider two wells $B_j = B(\bar{x}_j, \delta)$ with $x_1 = (\frac{1}{4}, \frac{3}{4})$, $x_2 = (\frac{3}{4}, \frac{1}{4})$ and the radius $\delta = 10^{-5}$. In the computations, we take $q_1 = -1$ and $q_2 = 1$ which corresponds to the situation that the well B_1 is an extraction well and B_2 is an injection well.

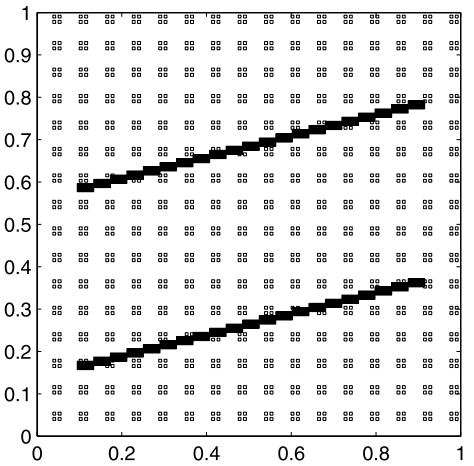

Fig. 7. Permeability field: $a^\epsilon = 10^5$ in two channels consisting of dark small rectangles; $a^\epsilon = 8 \times 10^4$ in small square inclusions; $a^\epsilon = 1$ otherwise.

Table 6
Relative errors for the model problem with the permeability depicted in Fig. 7. $\rho = h = 1/1024$, $\tilde{d} = H = 1/32$, $\gamma_0 = 20$, $\gamma_1 = 0.1$.

Relative error	L^2	L^∞	Energy norm
FEM	0.3339e−00	0.4615e−00	0.8511e+02
MsPGM	0.3551e−00	0.4011e−00	0.5946e−00
Mixed basis MsPGM	0.2477e−00	0.2670e−00	0.4999e−00
FE-OMsFEM	0.4786e−02	0.1362e−01	0.9322e−01
FE-OMsPGM	0.7510e−02	0.1931e−01	0.7857e−01

Table 7
Results of WBP and relative error with coefficient defined by (4.5). $\rho = \epsilon = 1/64$, $\tilde{d} = H = 1/64$, $h = 1/2048$, $\gamma_0 = 20$, $\gamma_1 = 0.1$.

Methods	Well 1		Well 2	
	WBP	Error	WBP	Error
MsPGM	−7.1895606	0.3342e−00	7.1895606	0.3342e−00
Mixed basis MsPGM	−5.8229884	0.8063e−01	6.1887201	0.1485e−00
G-MsFEM	−5.3838442	0.8635e−03	5.3739254	0.2704e−02
FE-OMsFEM	−5.4041646	0.2908e−02	5.4041646	0.2908e−02
FE-OMsPGM	−5.3843102	0.7770e−03	5.3843102	0.7770e−03

First, we assume the coefficient is

$$\mathbf{a}^\epsilon(x_1, x_2) = \frac{1}{(2 + 1.5 \sin \frac{2\pi x_1}{\epsilon})(2 + 1.5 \sin \frac{2\pi x_2}{\epsilon})}. \tag{4.5}$$

The exact solution of the problem is unknown and so we compute the "exact" solution using the method introduced in [35, Section 6] based on the well resolved solution on a uniform 2048×2048 mesh. In this test, we take $\epsilon = 1/64$, the "exact" well bore pressures are $\alpha_1 = -5.3884973$ in the first well and $\alpha_2 = 5.3884973$ in the second well (see [35, Example 7.1]).

In this test, both FE-OMsPGM and FE-OMsFEM are implemented via refining the coarse-grid elements around the wells as well as the union of coarse-grid elements adjacent to the boundary $\partial\Omega$. We also show the results obtained by the Algorithm 7.1 in [35], where the method needs to compute the discrete Green functions in a very fine mesh. We refer this method as G-MsFEM which uses the developed new Peaceman method to compute the WBPs (see [35, Section 6]). For other methods, we use the Peaceman model [53,54] to compute the WBPs on each well instead of the developed new Peaceman method since the bilinear form $A_\beta(\cdot,\cdot)$ of our method is nonsymmetric. The results are listed in Table 7. We can see that our FE-OMsPGM provides a better approximation of the WBP than G-MsFEM, and a much better approximation than the other methods in this example.

Next, we test the performance of our method for a random log-normal permeability field. We generate the random field $\mathbf{a}(x)$ on a uniform 1024×1024 mesh by using the technique in [52]. Fig. 8 shows a realization of the random permeability field. The "exact" well bore pressures of the two wells are $\alpha_1 = -0.9860407$ and $\alpha_2 = 4.6507305$ respectively.

Table 8 shows the results computed by using different methods. We observe that the introduced FE-OMsPGM provides a better approximation of the well bore pressure as well as FE-OMsFEM, and a much better approximation than the other methods in this example. In Fig. 9 we show the contour plots of the pressure field and the zoom region near-well computed by FE-OMsPGM on the 1024×1024 mesh. As a comparison, we show in Fig. 10 the contour plots of the "exact" pressure

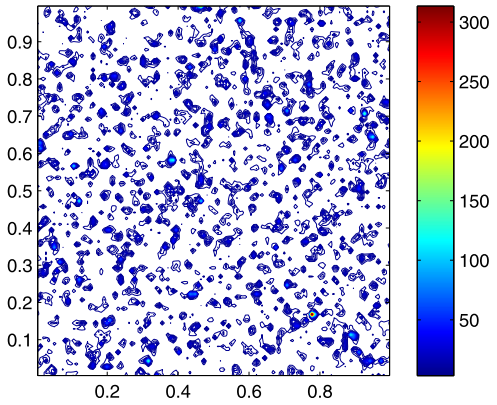

Fig. 8. The random log-normal permeability field $\mathbf{a}(x)$. $\frac{a_{\max}(x)}{a_{\min}(x)} = 6.06629\text{e}{+003}$.

Table 8
Results of WBP and relative error for the case of random log-normal field with $\sigma^2 = 1.0$ and $l_1 = l_2 = 0.01$. $\rho = h = 1/1024$, $\tilde{d} = H = 1/64$, $\gamma_0 = 10$, $\gamma_1 = 0.1$.

Methods	Well 1		Well 2	
	WBP	Error	WBP	Error
MsPGM	−0.9279028	0.5896e−01	4.2958017	0.7632e−01
Mixed basis MsPGM	−0.8932050	0.9415e−01	4.3157896	0.7209e−01
FE-OMsFEM	−0.9964647	0.1057e−01	4.6742562	0.5058e−02
FE-OMsPGM	−0.9701813	0.1608e−01	4.6391148	0.2498e−02

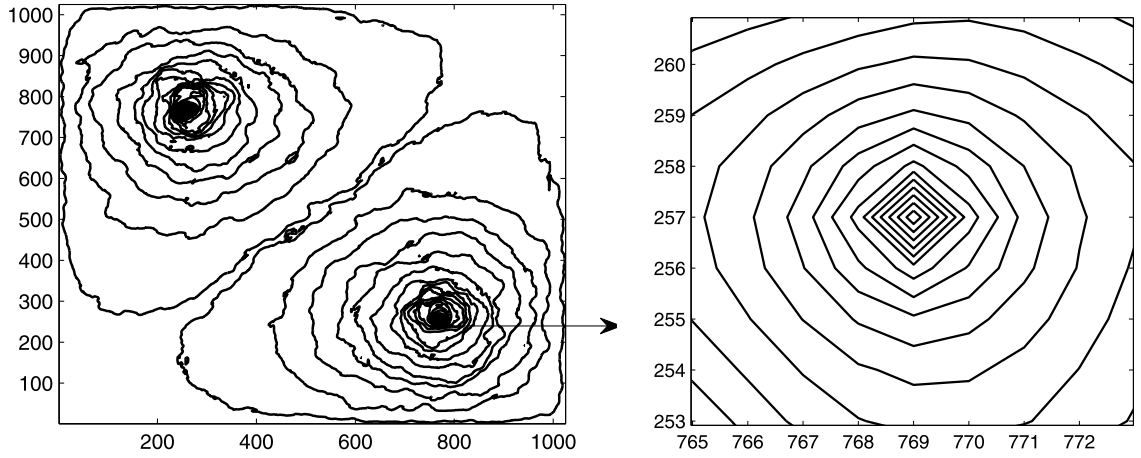

Fig. 9. Contour plots of the pressure field on the 1024×1024 mesh and the zoom region near-well by using FE-OMsPGM.

field and the zoom region near-well on the 1024×1024 mesh. We observe from these figures and Table 8 that our method provides good approximation of the well bore pressure as well as the large scale structure of the "exact" solutions for random log-normal permeability field.

5. Conclusion

In this paper, we have proposed a new numerical method for the multiscale elliptic problems with singularities which joints the oversampling MsPGM and the standard FEM by using the penalty techniques. The main purpose of this paper is to better approximate the singular features that occur in some special portions of the considered multiscale problem, e.g., the porous media with channelized structure, or in near-well region. For this goal, we first separate the research domain into two parts Ω_1 and $\Omega_2 = \Omega \setminus \overline{\Omega_1}$ that Ω_1 contains singular points (or regions) where the oversampling MsPGM is inefficient. Then we use the standard FEM on a fine mesh of Ω_1 and use the OMsPGM on a coarse mesh of Ω_2. In addition, we deal with the transmission condition on the interface $\Gamma = \partial\Omega_1 \cap \partial\Omega_2$ by penalizing the jumps from the linear function values as well as the fluxes of the discrete solution.

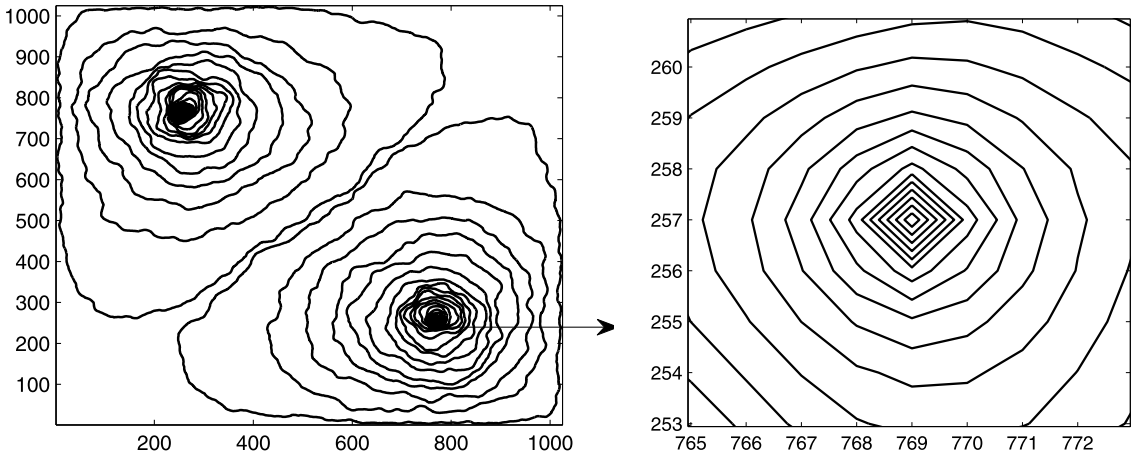

Fig. 10. Contour plots of the "exact" pressure field on the 1024×1024 mesh and the zoom region near-well.

Under some assumptions on the multiscale coefficient, we analyze the error between the fine grid solution and the FE-OMsPGM solution in the H^1 norm. Several numerical examples have been given to demonstrate the accuracy and efficiency of the proposed method. In particular, it is shown that the FE-OMsPGM gives highly effective approximation for the problems with singularities.

It is well known that each method has its own advantages and disadvantages. For example, the classical FEM can resolve fine features of the exact solution with enough DOFs but may exceed the computer capacity in large-scale multiscale simulations. The MsFEMs (including OMsPGM) construct the basis functions of the trial spaces by solving local problems with the same coefficient as the original multiscale problem, so that the basis functions can inherit fine information of the exact solution, and the resulting stiffness matrix is much smaller than that of FEM. But near the singularities, the multiscale basis functions may lose the solution structures which degenerate the performance of MsFEMs, while the FEM possesses many techniques such as adaptive algorithm (h, p, or hp refinements). So here the initial motivation of this paper comes: Why not to combine the two methods together to take advantages of the two methods? As a result, we obtained the FE-OMsPGM which uses much less DOFs than the standard FEM and may be more accurate than the OMsPGM for problems with singularities. The authors think the FE-OMsPGM is something between FEM and OMsPGM. It offers an option or a compromise to the readers who want to use more computer resource than MsPGM to obtain more accuracy than it. Although some kind of singularities such as high-contrast flow problems can be dealt with by the adaptive generalized multiscale finite element method (GMsFEM) [36], it also important to have FEM and MsFEM coupling. We think some of these ideas can be helpful in combining different MsFE basis functions.

Acknowledgements

The authors would like to thank the referees for their carefully reading and constructive comments that improved the paper.

Appendix A. Proofs of Lemma 3.2 and Theorem 3.1

Proof of Lemma 3.2. By (3.12), we have the asymptotic expansion

$$v_H = v_H^0 + \epsilon \chi^k(x/\epsilon)\frac{\partial v_H^0}{\partial x_k} + \epsilon \eta^k \frac{\partial v_H^0}{\partial x_k} \quad \text{on } K, \tag{A.1}$$

where $v_H^0 = \Pi_H v_H \in V_H$. Thus from (3.14) and $\left|\nabla \chi^k\right| \lesssim \epsilon^{-1}$, we have

$$\begin{aligned} \|\nabla v_H\|_{L^2(K)} &\leq \left\|\nabla v_H^0\right\|_{L^2(K)} + C\left(1 + \frac{\epsilon}{d_{S(K)}}\right)\left\|\nabla v_H^0\right\|_{L^2(K)} \\ &\leq C\left(1 + \frac{\epsilon}{d_{S(K)}}\right)\left\|\nabla v_H^0\right\|_{L^2(K)} \\ &\lesssim \left\|\nabla v_H^0\right\|_{L^2(K)}, \end{aligned} \tag{A.2}$$

which combines with the result of Lemma 5.1 in [37] yields (3.16) immediately. Further, from the proof of Lemma 5.1 in [37], we have

$$\alpha^* \left\| \nabla v_H^0 \right\|_{L^2(K)}^2 \le \left| \int_K \mathbf{a}^\epsilon \nabla v_H \cdot \nabla \Pi_H v_H \right| + \frac{\epsilon}{H_K} \left\| \nabla v_H^0 \right\|_{L^2(K)}^2,$$

where α^* is a positive constant such that $\xi_i a_{ij}^* \xi_j \ge \alpha^* |\xi|^2, \forall \xi \in \mathbb{R}^n$ since the homogenized coefficient $\mathbf{a}^*$ is positive definite (see [48]). Hence, by assuming that $\frac{\epsilon}{H_K}$ is sufficiently small, we obtain

$$C \left\| \nabla v_H^0 \right\|_{L^2(K)}^2 \le \left| \int_K \mathbf{a}^\epsilon \nabla v_H \cdot \nabla \Pi_H v_H \right|,$$

which combined with (3.16) yields the left inequality of (3.17) immediately. The right inequality of (3.17) can be proved by the Cauchy–Schwarz inequality and (3.16) directly. □

To begin the proof of Theorem 3.1, we first introduce the Scott–Zhang interpolation operator $Z_h : H^1(\Omega_1) \to V_h$. For any node z in $\mathcal{T}_{h,1}$, let $\phi_z(x)$ be the nodal basis function associated with z and let e_z be an edge/face with one vertex at z, then the Scott–Zhang interpolation operator is defined as [55]:

$$Z_h v = \sum_{\text{node } z \text{ in} \mathcal{T}_{h,1}} \left(\int_{e_z} \psi_z v \right) \phi_z \quad \forall v \in H^1(\Omega_1), \tag{A.3}$$

where $\psi_z(x)$ is a linear function that satisfies $\int_{e_z} \psi_z(x) w(x) = w(z)$ for any linear function $w(x)$ on e_z. Suppose $e_z \subset \partial\Omega_1$ for $z \in \partial\Omega_1$ and $e_z \subset \Omega_{\Gamma_h}$ for $z \in \Omega_{\Gamma_h}$, where Ω_{Γ_h} is defined in (3.4). This operator enjoys the following stability and interpolation estimates (see [55]):

Lemma A.1. *For any $K \in \mathcal{T}_{h,1}$, we have*

$$\|Z_h v\|_{L^\infty(K)} \lesssim \|v\|_{L^\infty(\tilde{K})}, \|\nabla Z_h v\|_{L^p(K)} \lesssim \|\nabla v\|_{L^p(\tilde{K})}, p = 2, \infty. \tag{A.4}$$

$$\|v - Z_h v\|_{L^2(K)} + h_K \|v - Z_h v\|_{H^1(K)} \lesssim h_K^2 |v|_{H^2(\tilde{K})}, \tag{A.5}$$

where $\tilde{K}$ is the union of all elements in $\mathcal{T}_{h,1}$ having nonempty intersection with K.

Proof of Theorem 3.1. According to Lemma 3.5, the proof is divided into two parts. The first part is devoted to estimating the interpolation error. To do this, we take

$$\phi_H^K = \sum_{x_i^K \text{ node of } K} u_0(x_i^K) \bar{\psi}_i^K(x), \tag{A.6}$$

and define ψ_H by

$$\psi_H|_K = \phi_H^K \quad \forall K \in \mathcal{T}_{H,2}. \tag{A.7}$$

Clearly, $\psi_H \in V_{H,nc}^{ms}$. It is easy to see that

$$\Pi_K \phi_H^K = I_H u_0,$$

where $I_H : C(\bar{\Omega}_2) \to V_H$ is the standard Lagrange interpolation operator over linear finite element space. Then we set $v_{h,H}$ as $v_{h,H}|_{\Omega_1} = \hat{u}_h$, $v_{h,H}|_{\Omega_2} = \psi_H$, where $\hat{u}_h := Z_h(u_1 + \epsilon\theta_\epsilon)$, and ψ_H is defined by (A.7). It is shown that in [37, pp. 1443–1447],

$$\begin{aligned} &\Bigg(\sum_{K \in \mathcal{T}_{h,H}} \|(\mathbf{a}^\epsilon)^{1/2} \nabla(u_\epsilon - v_{h,H})\|_{L^2(K)}^2 + \sum_{e \in \Gamma_h} \frac{\epsilon}{\gamma_0} \left\| \left\{ \mathbf{a}^\epsilon \nabla(u_\epsilon - v_{h,H}) \cdot \mathbf{n} \right\} \right\|_{L^2(e)}^2 \\ &\quad + \sum_{e \in \Gamma_h} \gamma_1 \epsilon \left\| \left[\mathbf{a}^\epsilon \nabla(u_\epsilon - v_{h,H}) \cdot \mathbf{n} \right] \right\|_{L^2(e)}^2 \Bigg)^{1/2} \\ &\lesssim H |u_0|_{H^2(\Omega)} + \sqrt{\epsilon} |u_0|_{W^{1,\infty}(\Omega)} + \frac{\epsilon}{d} |u_0|_{W^{1,\infty}(\Omega_2)} + \frac{h}{\epsilon} |\Omega_1|^{\frac{1}{2}} |u_0|_{W^{1,\infty}(\Omega_1)} + \epsilon^2 \|\nabla f\|_{L^2(\Omega_\Gamma)}. \end{aligned} \tag{A.8}$$

It remains to consider the term $\sum_{e \in \Gamma_h} \frac{\gamma_0}{\epsilon} \left\| \left[u_\epsilon - \Pi v_{h,H} \right] \right\|_{L^2(e)}^2$. Noting that both u_ϵ and u_0 are continuous functions, we have

$$\begin{aligned}\sum_{e\in\Gamma_h}\frac{\gamma_0}{\epsilon}\left\|\left[u_\epsilon-\Pi v_{h,H}\right]\right\|^2_{L^2(e)} &= \sum_{e\in\Gamma_h}\frac{\gamma_0}{\epsilon}\int_e\left[u_0-\Pi v_{h,H}\right]^2\\ &\lesssim \sum_{E\in\Gamma_H}\frac{\gamma_0}{\epsilon}\int_E(u_0-\Pi\psi_H)^2+\sum_{e\in\Gamma_h}\frac{\gamma_0}{\epsilon}\int_e(u_0-Z_hu_0)^2\\ &\quad+\sum_{e\in\Gamma_h}\frac{\gamma_0}{\epsilon}\int_e\left(Z_h\left(\epsilon\chi^j\frac{\partial u_0}{\partial x_j}\right)\right)^2+\sum_{e\in\Gamma_h}\frac{\gamma_0}{\epsilon}\int_e\epsilon^2(Z_h\theta_\epsilon)^2\\ &:= \mathrm{R}_1+\mathrm{R}_2+\mathrm{R}_3+\mathrm{R}_4.\end{aligned}$$

From the definitions of Π_K and Π, we have that $\Pi\phi_H^K=\Pi_K\phi_H^K=I_Hu_0$. Then, by use of Lemma 3.1, we have

$$\begin{aligned}\int_E(u_0-\Pi\psi_H)^2 &= \int_E(u_0-I_Hu_0)^2\\ &\lesssim H^{-1}\left\|u_0-I_Hu_0\right\|^2_{L^2(K_E)}+\left\|u_0-I_Hu_0\right\|_{L^2(K_E)}\left\|\nabla(u_0-I_Hu_0)\right\|_{L^2(K_E)}\\ &\lesssim H^3|u_0|^2_{H^2(K_E)},\end{aligned}$$

which yields

$$\mathrm{R}_1\lesssim\frac{H^3}{\epsilon}|u_0|^2_{H^2(\Omega_{\Gamma_H})} \tag{A.9}$$

Similarly, from Lemmas 3.1 and A.1, we have

$$\begin{aligned}\int_e(u_0-Z_hu_0)^2 &\lesssim h^{-1}\left\|u_0-Z_hu_0\right\|^2_{L^2(K_e)}+\left\|u_0-Z_hu_0\right\|_{L^2(K_e)}\left\|\nabla(u_0-Z_hu_0)\right\|_{L^2(K_e)}\\ &\lesssim h^3|u_0|^2_{H^2(\tilde{K}_e)},\end{aligned}$$

which yields

$$\mathrm{R}_2\lesssim\frac{h^3}{\epsilon}|u_0|^2_{H^2(\Omega_{\Gamma_h})} \tag{A.10}$$

Further, from Lemma A.1, it is easy to see that

$$\begin{aligned}\int_e\left(Z_h\left(\epsilon\chi^j\frac{\partial u_0}{\partial x_j}\right)\right)^2 &\lesssim h_e\epsilon^2\left\|Z_h\left(\chi^j\frac{\partial u_0}{\partial x_j}\right)\right\|^2_{L^\infty(K_e)}\\ &\lesssim h_e\epsilon^2\left\|\chi^j\frac{\partial u_0}{\partial x_j}\right\|^2_{L^\infty(\tilde{K}_e)}\\ &\lesssim h_e\epsilon^2\left\|\frac{\partial u_0}{\partial x_j}\right\|^2_{L^\infty(\tilde{K}_e)},\end{aligned}$$

which yields

$$\mathrm{R}_3\lesssim\epsilon|u_0|^2_{W^{1,\infty}(\Omega_1)} \tag{A.11}$$

In addition, from (A.3) and noting that $e_z\subset\Gamma$ for $z\in\Gamma$, we have

$$\mathrm{R}_4\lesssim\epsilon\left\|Z_h\theta_\epsilon\right\|^2_{L^\infty(\Gamma)}\lesssim\epsilon\left\|\theta_\epsilon\right\|^2_{L^\infty(\Gamma)}\lesssim\epsilon\left|u_0\right|^2_{W^{1,\infty}(\Omega)}, \tag{A.12}$$

where we have used (3.9) to derive the last inequality. Thus, from (A.9)–(A.12), it follows that

$$\sum_{e\in\Gamma_h}\frac{\gamma_0}{\epsilon}\int_e\left[u_\epsilon-\Pi v_{h,H}\right]^2\lesssim\frac{H^3}{\epsilon}|u_0|^2_{H^2(\Omega_{\Gamma_H})}+h^2|u_0|^2_{H^2(\Omega_{\Gamma_h})}+\epsilon|u_0|^2_{W^{1,\infty}(\Omega)}. \tag{A.13}$$

From the definition of Ω_Γ (see (3.1)) and the assumption (H1), we have $|\Omega_\Gamma|=O(H)$. Hence, from (A.13) and (A.8), it follows (3.24) immediately. This completes the proof. □

References

[1] M. Dorobantu, B. Engquist, Wavelet-based numerical homogenization, SIAM J. Numer. Anal. 35 (1998) 540–559.
[2] W. E, B. Engquist, The heterogeneous multiscale methods, Commun. Math. Sci. 1 (2003) 87–132.
[3] W. E, B. Engquist, Multiscale modeling and computation, Not. Am. Math. Soc. 50 (2003) 1062–1070.
[4] W. E, P. Ming, P. Zhang, Analysis of the heterogeneous multiscale method for elliptic homogenization problems, J. Am. Math. Soc. 18 (2005) 121–156.
[5] C.L. Farmer, Upscaling: a review, in: Proceedings of the Institute of Computational Fluid Dynamics Conference on Numerical Methods for Fluid Dynamics, Oxford, UK, 2001.
[6] X.H. Wu, Y. Efendiev, T. Hou, Analysis of upscaling absolute permeability, Discrete Contin. Dyn. Syst., Ser. B (2002) 185–204.
[7] G. Sangalli, Capturing small scales in elliptic problems using a residual-free bubbles finite element method, SIAM MMS 1 (2003) 485–503.
[8] T. Hughes, Multiscale phenomena: Green's functions, the Dirichlet to Neumann formulation, subgrid scale models, bubbles and the origin of stabilized methods, Comput. Methods Appl. Mech. Eng. 127 (1995) 387–401.
[9] J. Fish, Z. Yuan, Multiscale enrichment based on partition of unity, Int. J. Numer. Methods Eng. 62 (2005) 1341–1359.
[10] L.P. Franca, A. Russo, Deriving upwinding, mass lumping and selective reduced integration by residual-free bubbles, Appl. Math. Lett. 9 (5) (1996) 83–88.
[11] B. Engquist, O. Runborg, Wavelet-based numerical homogenization with applications, in: T. Barth, T. Chan, R. Heimes (Eds.), Multiscale and Multiresolution Methods: Theory and Applications, in: Lecture Notes in Computational Sciences and Engineering, vol. 20, Springer-Verlag, Berlin, 2002, pp. 97–148.
[12] F. Brezzi, L.P. Franca, T.J.R. Hughes, A. Russo, $b = \int g$, Comput. Methods Appl. Mech. Eng. 145 (1997) 329–339.
[13] Y. Efendiev, T.Y. Hou, X.H. Wu, Convergence of a nonconforming multiscale finite element method, SIAM J. Numer. Anal. 37 (2000) 888–910.
[14] T.Y. Hou, X.H. Wu, A multiscale finite element method for elliptic problems in composite materials and porous media, J. Comput. Phys. 134 (1997) 169–189.
[15] T.Y. Hou, X.H. Wu, Z. Cai, Convergence of a multiscale finite element method for elliptic problems with rapidly oscillation coefficients, Math. Comput. 68 (1999) 913–943.
[16] Y. Efendiev, T.Y. Hou, V. Ginting, Multiscale finite element methods for nonlinear partial differential equations, Commun. Math. Sci. 2 (4) (2004) 553–589.
[17] Y. Efendiev, A. Pankov, Numerical homogenization of nonlinear random parabolic operators, SIAM MMS 2 (2) (2004) 237–268.
[18] Y. Efendiev, T. Hou, Multiscale finite element methods for porous media flows and their applications, Appl. Numer. Math. 57 (5–7) (2007) 577–596.
[19] Y. Efendiev, V. Ginting, T.Y. Hou, R. Ewing, Accurate multiscale finite element methods for two-phase flow simulations, J. Comput. Phys. 220 (1) (2006) 155–174.
[20] T.Y. Hou, X.H. Wu, Y. Zhang, Removing the cell resonance error in the multiscale finite element method via a Petrov–Galerkin formulation, Commun. Math. Sci. 2 (2) (2004) 185–205.
[21] Z. Chen, T.Y. Hou, A mixed multiscale finite method for elliptic problems with oscillating coefficients, Math. Comput. 72 (2002) 541–576.
[22] J.E. Aarnes, On the use of a mixed multiscale finite element method for greater flexibility and increased speed or improved accuracy in reservoir simulation, SIAM MMS 2 (2004) 421–439.
[23] J.E. Aarnes, Y. Efendiev, Mixed multiscale finite element methods for stochastic porous media flows, SIAM J. Sci. Comput. 30 (2008) 2319–2339.
[24] J.E. Aarnes, Y. Efendiev, L. Jiang, Mixed multiscale finite element methods using limited global information, SIAM MMS 7 (2008) 655–676.
[25] W. Deng, X. Yun, C. Xie, Convergence analysis of the multiscale method for a class of convection–diffusion equations with highly oscillating coefficients, Appl. Numer. Math. 59 (2009) 1549–1567.
[26] P. Jenny, S. Lee, H. Tchelepi, Multi-scale finite-volume method for elliptic problems in subsurface flow simulation, J. Comput. Phys. 187 (1) (2003) 47–67.
[27] C.-C. Chu, I.G. Graham, T.-Y. Hou, A new multiscale finite element method for high-contrast elliptic interface problems, Math. Comput. 79 (272) (2010) 1915–1955.
[28] Y. Efendiev, J. Galvis, X.H. Wu, Multiscale finite element methods for high-contrast problems using local spectral basis functions, J. Comput. Phys. 230 (4) (2011) 937–955.
[29] Y. Efendiev, T.Y. Hou, Multiscale Finite Element Methods Theory and Applications, Springer, Lexington, KY, 2009.
[30] A. Gloria, Reduction of the resonance error—Part 1: Approximation of homogenized coefficients, Math. Models Methods Appl. Sci. 21 (8) (2011) 1601–1630.
[31] P. Henning, D. Peterseim, Oversampling for the multiscale finite element method, Multiscale Model. Simul. 11 (4) (2013) 1149–1175.
[32] J. Galvis, Y. Efendiev, Domain decomposition preconditioners for multiscale flows in high-contrast media, SIAM MMS 8 (2010) 1461–1483.
[33] J. Galvis, Y. Efendiev, Domain decomposition preconditioners for multiscale flows in high-contrast media: reduced dimension coarse spaces, SIAM MMS 8 (2010) 1621–1644.
[34] H. Owhadi, L. Zhang, Localized bases for finite-dimensional homogenization approximations with nonseparated scales and high contrast, SIAM MMS 9 (2011) 1373–1398.
[35] Z. Chen, X.Y. Yue, Numerical homogenization of well singularities in the flow transport through heterogeneous porous media, SIAM MMS 1 (2003) 260–303.
[36] E.T. Chung, Y. Efendiev, G. Li, An adaptive GMsFEM for high-contrast flow problems, J. Comput. Phys. 273 (2014) 54–73.
[37] W. Deng, H. Wu, A combined finite element and multiscale finite element method for the multiscale elliptic problems, Multiscale Model. Simul. 12 (4) (2014) 1424–1457.
[38] D. Arnold, An interior penalty finite element method with discontinuous elements, SIAM J. Numer. Anal. 19 (1982) 742–760.
[39] D. Arnold, F. Brezzi, B. Cockburn, D. Marini, Unified analysis of discontinuous Galerkin methods for elliptic problems, SIAM J. Numer. Anal. 39 (2001) 1749–1779.
[40] I. Babuška, M. Zlámal, Nonconforming elements in the finite element method with penalty, SIAM J. Numer. Anal. 10 (5) (1973) 863–875.
[41] G. Baker, Finite element methods for elliptic equations using nonconforming elements, Math. Comput. 31 (1977) 44–59.
[42] A. Målqvist, D. Peterseim, Localization of elliptic multiscale problems, Math. Comput. 83 (290) (2014) 2583–2603.
[43] P. Henning, M. Ohlberger, B. Schweizer, An adaptive multiscale finite element method, Multiscale Model. Simul. 12 (2014) 1078–1107.
[44] D. Elfverson, E.H. Georgoulis, A. Målqvist, D. Peterseim, Convergence of a discontinuous Galerkin multiscale method, SIAM J. Numer. Anal. 51 (6) (2013) 3351–3372.
[45] D. Elfverson, A discontinuous Galerkin multiscale method for convection–diffusion problems, in press.
[46] Z. Chen, H. Wu, Selected Topics in Finite Element Method, Science Press, Beijing, 2010.
[47] A. Bensoussan, J.L. Lions, G. Papanicolaou, Asymptotic Analysis for Periodic Structure, Studies in Mathematics and Its Application, vol. 5, North-Holland Publ., 1978.
[48] V.V. Jikov, S.M. Kozlov, O.A. Oleinik, Homogenization of Differential Operators and Integral Functionals, Springer-Verlag, Berlin, 1994.
[49] O.A. Ladyzhenskaia, N.N. Uraltseva, Linear and Quasilinear Elliptic Equations, Academic Press, New York, 1968.
[50] S.C. Brenner, L.R. Scott, The Mathematical Theory of Finite Element Methods, Springer-Verlag, New York, 2002.

[51] P.G. Ciarlet, The Finite Element Method for Elliptic Problems, North Holland, Amsterdam, 1978.
[52] L. Durlofsky, Numerical calculation of equivalent grid block permeability tensors for heterogeneous porous media, Water Resour. Res. 27 (1991) 699–708.
[53] D.W. Peaceman, Interpretation of well-block pressures in numerical reservoir simulations, Soc. Pet. Eng. J. 18 (1978) 183–194.
[54] D.W. Peaceman, Interpretation of well-block pressures in numerical reservoir simulations with non-square grid blocks and anisotropic permeability, Soc. Pet. Eng. J. 23 (1983) 531–543.
[55] R. Scott, S. Zhang, Finite element interpolation of nonsmooth functions satisfying boundary conditions, Math. Comput. 54 (190) (1990) 483–493.